

Representative volume elements for matrix-inclusion composites - a computational study on periodizing the ensemble

Matti Schneider^{1,*}, Marc Josien², and Felix Otto³

¹Karlsruhe Institute of Technology (KIT), Institute of Engineering Mechanics

²CEA, DES, IRESNE, DEC, Cadarache, F-13108, Saint-Paul-Lez-Durance, France

³Max-Planck Institute for Mathematics in the Sciences (MPI MiS)

*correspondence to: matti.schneider@kit.edu

March 16, 2021

Abstract

We investigate volume-element sampling strategies for the stochastic homogenization of particle-reinforced composites and show, via computational experiments, that an improper treatment of particles intersecting the boundary of the computational cell may affect the accuracy of the computed effective properties. Motivated by recent results on a superior convergence rate of the systematic error for periodized ensembles compared to taking snapshots of ensembles, we conduct computational experiments for microstructures with circular, spherical and cylindrical inclusions and monitor the systematic errors in the effective thermal conductivity for snapshots of ensembles compared to working with microstructures sampled from periodized ensembles.

We observe that the standard deviation of the apparent properties computed on microstructures sampled from the periodized ensembles decays at the scaling expected from the central limit theorem. In contrast, the standard deviation for the snapshot ensembles shows an inferior decay rate at high filler content. The latter effect is caused by additional long-range correlations that necessarily appear in particle-reinforced composites at high, industrially relevant, volume fractions. Periodized ensembles, however, appear to be less affected by these correlations.

Our findings provide guidelines for working with digital volume images of material microstructures and the design of representative volume elements for computational homogenization.

Keywords: Quantitative stochastic homogenization; FFT-based computational homogenization; Thermal conductivity; Screening the boundary-layer error; Microstructure modeling

1 Introduction

1.1 State of the art

The concept of representative volume element (RVE) plays a central role for predicting the effective properties of random heterogeneous materials. Originally, Hill [1] defined an RVE as a bounded domain that is statistically typical of the mixture and sufficiently large to render the effects of artificially imposed boundary conditions negligible. Drugan & Willis [2] improved upon the original concept by relaxing the previous definition, that requires the RVE to be typical for *all* statistics of interest. Rather, they focused on the material properties and defined an RVE as a bounded domain whose apparent properties are sufficiently close to the effective properties of the infinitely large medium. This shift in paradigm, which introduced the infinite-volume limit as a suitable reference quantity, enabled much smaller RVEs to be used, with obvious advantages in terms of computational complexity. Kanit et al. [3] proposed a more quantitative definition of the RVE based on the statistics of the apparent properties on cells of varying, but finite, size. They introduced the notions of bias and dispersion (corresponding to the systematic and the random error, respectively, to be discussed below) for the apparent properties, and provided theoretical arguments as well as empirical data in support of using several realizations of the ensemble on smaller volumes to arrive at the same accuracy as for a single "large" RVE. Improvements in computational power and algorithmic advances gave significant impetus to modern multiscale methods in engineering, also dealing with nonlinear and time-dependent problems, see Matouš et al. [4] for a recent overview.

In general, one may distinguish two succinctly different strategies for acquiring the microstructures necessary for multiscale methods in engineering. On the one hand, synthetic microstructures may be generated based on statistical data available on the material under consideration, see Bargmann et al. [5] for a recent overview. On the other hand, digital volume images of real microstructures [6,7] may be obtained directly, serving as what we call snapshots of the random material. Both approaches complement each other, and may be used cooperatively. Indeed, synthetic microstructures offer full control over the ensemble, and thorough RVE studies can be conducted. However, the relation of these synthetic structures to their real counterparts is not always apparent. In contrast, snapshots are real, but their acquisition is typically costly, which makes it hard to study their representativity and to quantify the underlying uncertainty.

Parallel to developments in engineering, homogenization theory was established as a rigorous foundation for the up-scaling of random heterogeneous media. Building upon previous work in the periodic setting [8–10], Varadhan & Papanicolaou [11] and Kozlov [12] established qualitative results for stochastic homogenization for stationary and ergodic ensembles of coefficient fields. In this context and informally speaking, stationarity means that the statistical properties of the ensembles are translation-invariant, whereas ergodicity means that the microstructure becomes statistically independent over distances tending to infinity.

Classically, the effective properties in stochastic homogenization are defined by spatially averaging so-called corrector fields which are defined on the whole space. The RVE methodology, i.e., working with cells of large but finite size, is imperative from a computational point of view. The error of the apparent property associated to single finite-sized cell compared to the true effective properties of stochastic homogenization naturally decomposes into two parts [13, Eq. (13)]. The random error quantifies the fluctuation of the apparent properties on cells of fixed size, whereas the systematic error measures the deviation of the expectation of the apparent property on cells of fixed size from the true effective property. These two error contributions correspond to the bias and dispersion considered by Kanit et al. [3]. Theoretical guarantees that the systematic as well as the random error converge to zero as the cell size goes to infinity were provided by Bourgeat & Piatnitski [14] and Owhadi [15] for Dirichlet, Neumann and

periodic boundary conditions imposed on the boundary of the considered cells.

These results hold in the general setting of stationary and ergodic random media. Thus, they may only provide *qualitative* convergence results, i.e., convergence of the random and the systematic error to zero, without rates. To obtain specific convergence rates, the correlation properties of the coefficient field need to be quantified, see Section 2 below for a discussion.

Theoretical works also shed some light on the two different approaches for obtaining microstructures discussed earlier. For the mathematical analysis, the full ensemble of microstructures needs to be given, and its stochastic properties are encoded by the underlying correlation structure. Acquiring snapshots corresponds to drawing a specific sample of the ensemble, and restricting the microstructure to a cell of finite size. This approach is straightforward, and is tacitly assumed in the qualitative convergence results [14, 15]. Generating synthetic microstructures is more subtle, as those are typically generated on a rectangular cell with periodic boundary conditions, i.e., on a torus, mathematically speaking. Thus, these generated elements are more than simple restrictions of the infinite-space ensemble, but require the underlying "construction plan" to be known [16, Sec. 3.2.3], for instance via pushing forward a specific probability distribution by a (deterministic) mapping. With this more fundamental knowledge at hand, it is natural to draw samples from suitably periodized ensembles for the finitely sized cells. In practical engineering terms, microstructure-generation algorithms are - in principle - deterministic, but some of its input parameters are drawn from probability distributions. Combining the random input and the deterministic algorithm gives rise to the ensemble, and drawing samples from the periodized ensemble corresponds to working on the torus instead of a box in Euclidean space, for instance when computing distances or applying filters.

Over the years, in terms of theoretical reasoning as well as numerical evidence, it has been realized that the snapshot strategy may introduce non-negligible boundary effects compared to the periodization approach. This observation surfaced in numerical multiscale methods [17, 18], where the finite-element ansatz functions were modified in order to account for heterogeneity on a sub-element scale by solving a corrector-type equation with suitable boundary conditions. In the setting of periodic homogenization it was realized that working on cubic volume elements with an edge length L that is not an integer multiple of the period leads to an error in the effective properties that is of order $1/L$. To reduce this so-called resonance error, oversampling/filtering techniques [17, 19] were introduced. Alternative approaches screen the boundary effect by modifying the cell problem, for instance by adding a "massive", zero-th order term to the elliptic operator defining the corrector problem [20, Thm. 1]. In a similar spirit, screening strategies based on parabolic [21, 22] or hyperbolic [23] versions of the corrector problem have been considered. In the context of stochastic homogenization, the snapshot approach also gives rise to a boundary-layer error, just as for periodic homogenization with non-matching period. In the stochastic setting, Egloffé et al. [16, Eq. (3.4)] expected the systematic error to decay with the rate $1/L$, as for the periodic case. Recently, Clozeau et al. [24] provided a theoretical argument for the $1/L$ -scaling, at least in the asymptotic setting of vanishing material contrast. Because of the slow decay of the random boundary layer, filtering techniques are expected to have no effect on the scaling $1/L$ [25, Sec. 4]. However, screening by a massive term, in conjunction with extrapolation in the massive parameter, has been shown to reduce the systematic error to $1/L^d$ [13, Thm. 2]. Based on screening and extrapolation, Mourrat [22, Prop. 1.1 & Th. 1.2] devised a numerical algorithm that, on the basis of a snapshot, extracts the effective behavior up to the optimal total-error rate $1/L^{\frac{d}{2}}$ at the cost of on the order of L^d operations.

Hence, the most effective improvements in the decay of the boundary-layer error rest upon a modification of the corrector problem. However, from an engineering point of view, modifying the underlying partial differential equation for more general problems to be homogenized, e.g. elasticity or inelasticity, can only be a last resort, even if it improves the convergence rate. Apart from physical reasons, such an approach

requires modifying existing computational homogenization codes at their core.

Recently, Clozeau et al. [24] worked out the details of an attractive alternative to modifying the corrector problem. Instead, they modify the ensemble by periodizing it on cells of finite size, thus recovering the more favorable $1/L^d$ convergence rate of the systematic error (without modifying the corrector equation). This is in line with the existing bounds of Gloria et al. [13] and Egloffé et al. [16, Sec. 3.2.3], which concern i.i.d. random conductivities on a discrete lattice, and with Khoromskaia et al. [26], who investigated an ensemble based on a discrete Poisson point process numerically. However, periodizing the aforementioned ensembles is trivial; on the contrary, Clozeau et al. [24] deal with a less academic and more realistic class of ensembles, namely coefficient fields generated by applying a nonlinear transformation to a Gaussian field with (essentially) integrable correlation function. Moreover, Clozeau et al. [24] do not only provide an estimate of the systematic error but actually derive the leading-order term in L^{-d} , which is generically non-vanishing. For applications in engineering, the result [24] suggests that working with periodized ensembles leads to a favorable systematic error compared to the snapshot approach. This is very much in line with observations in engineering. For instance, considering Poisson-Voronoi microstructures, Kanit et al. [3, Sec. 7] observe that "the bias [systematic error] introduced by the periodic boundary conditions is found to be much smaller than for the other boundary conditions".

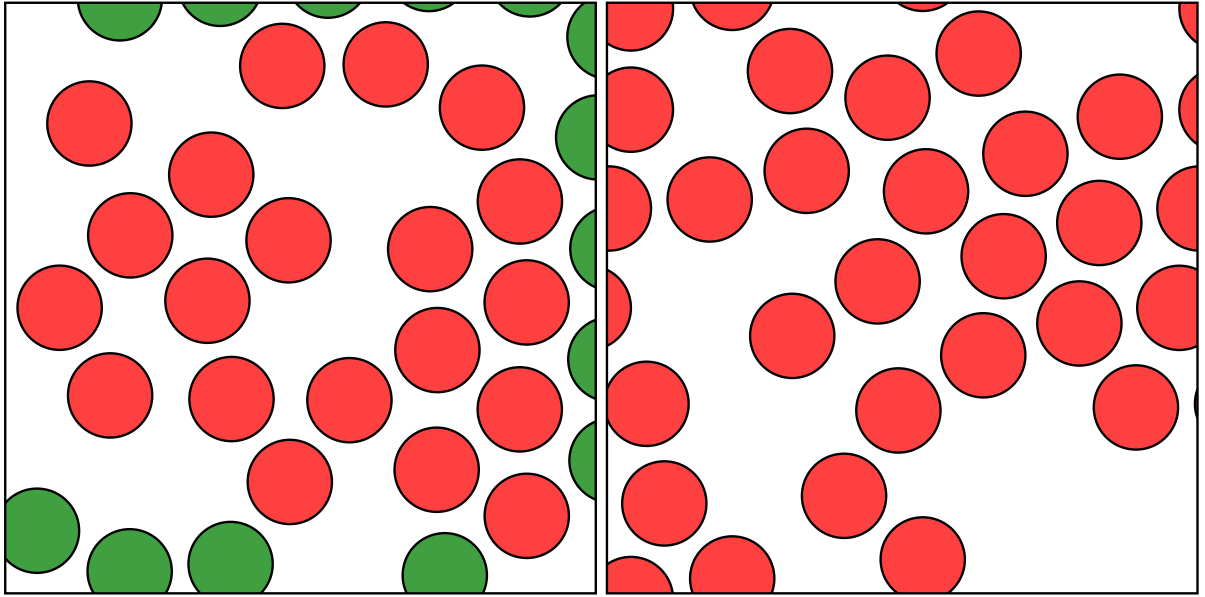
1.2 Contributions

We carry out numerical experiments to quantify the systematic and the random error for composite microstructures. In contrast to previous works [26,27], we use microstructures of industrial relevance and complexity, utilizing real physical parameters, investigating spherical and cylindrical fillers. While the ensembles considered here do not fall into the class considered in the theory - they are neither finite range nor a suitable functional inequality is known, see, however, Duerinckx & Gloria [28,29] - we expect that they belong to the same universality class. Thus, the composites under consideration serve as benchmarks for the established quantitative homogenization theory, and are expected to stimulate further theoretical research.

We are interested in the consequences of improper treatment of particles intersecting the boundary of computational volume elements, leading to the boundary-layer error, and compare these results to properly periodized ensembles.

From a practical engineering perspective, these results shed light on modern up-scaling techniques based on digital volume images, for instance obtained by micro-computed tomography. Indeed, the latter images naturally correspond to snapshots of ensembles with "improperly" treated particles at the boundaries. The effort of extracting such a specimen precludes computing the apparent properties corresponding to this cell size, as the necessary number of samples, which is typically on the order of 10^5 for engineering accuracy [26,27], is both too expensive and excessively arduous. For this purpose, we prepare a similar protocol under "laboratory conditions". More precisely, we consider the simplified scenario of thermal conductivity, but rely upon modern computational homogenization techniques based on the fast Fourier transform (FFT), pioneered by Moulinec & Suquet [30,31], and validated methods for generating synthetic microstructure-generation algorithms for spherical and cylindrical fillers [32,33] to quantify the effect of taking snapshots of random media on finite-sized cells.

In Section 2, we provide a streamlined presentation of quantitative stochastic homogenization suitable for readers with an engineering background. After exposing the microstructure-generation tools in Section 3, the computational results are presented in Section 4, comprising over 250 000 simulation runs with up to more than one billion degrees of freedom. An extensive discussion of the non-standard decay of the random error is provided in Section 5.



(a) Taking a snapshot introduces cut particles (green) in addition to original particles (red) (b) For a properly periodized ensemble, all inclusions belong to the same species

Figure 1: Illustrating snapshot coefficients A_L^{sn} vs. periodized coefficients A_L^{per}

2 Theoretical background

We are concerned with a stationary and ergodic random field of thermal conductivity tensors A in d spatial dimensions, i.e., every realization is a field on \mathbb{R}^d with values in symmetric positive definite $d \times d$ -matrices. In stochastic homogenization [11, 12], the effective conductivity tensor \bar{A} is sought, and may be determined for any prescribed (negative) temperature gradient $\bar{\xi} \in \mathbb{R}^d$ via the expectation of the heat flux

$$\bar{A}\bar{\xi} = \langle A\xi \rangle, \quad (2.1)$$

where ξ denotes the corresponding *local* (negative) temperature gradient, i.e.,

$$\xi = \bar{\xi} + \Gamma\xi \quad (2.2)$$

holds in terms of the Helmholtz projector Γ onto stationary gradient fields, and the associated heat flux $q = A\xi$ is divergence-free, i.e., the equation

$$\Gamma q = 0 \quad (2.3)$$

is satisfied. Due to the ergodicity assumption, the effective conductivity tensor \bar{A} may also be computed in terms of a single realization involving an infinite-volume limit, see Chapter 7 in Zhikov et al. [34] for details.

For computational purposes it is necessary to work on finite domains. For a fixed cube $Q_L = [-\frac{L}{2}, \frac{L}{2}]^d$, assume that we are given an ensemble A_L that generates coefficient fields on the cell Q_L . The latter can be obtained as snapshots of the random conductivity tensor field A , which is given on the whole space, on the cube Q_L . In this case, we will write A_L^{sn} for the corresponding ensemble. An alternative approach proceeds by *periodizing* the ensemble. In this case, we will denote the ensemble by A_L^{per} . Taking snapshots of an ensemble is straightforward because it can be performed on given realizations, whereas periodization is a more subtle process (to be discussed below) and requires working on the level of the ensemble itself. However, periodization is quite natural when generating synthetic microstructures.

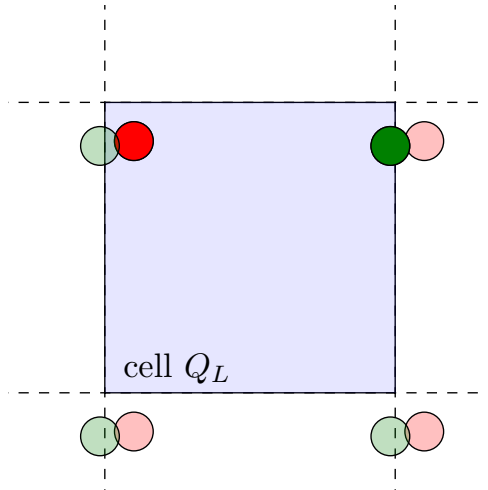


Figure 2: Periodizing the distance for a two-dimensional cell Q_L containing two circles (red and green) of equal radius and their shaded periodically replicated images

Let us illustrate what we mean by periodizing the ensemble. For i.i.d. discrete coefficient fields [13] and the Poissonian ensemble [35], this procedure is trivial. For Gaussian fields, periodization amounts to periodizing the correlation function, see Clozeau et al. [24]. For the article at hand, we consider a particle-reinforced composite with a single species of particles, for instance spherical particles, and specific macroscopic statistics. When taking a snapshot of the coefficient field on a box Q_L (thus building A_L^{sn}), particles intersecting the boundary of Q_L are cut, giving rise to another species of particles featuring its own statistics, see Fig. 1(a). In particular, taking snapshots of the particles does not retain the stationarity property of the whole-space ensemble.

To understand how periodization proceeds let us look at the way an ensemble of particle-filled composites is built. In real life, the fillers do not overlap (unless this is part of the production process, for instance in sintering). Thus, when generating an ensemble, an overlap check needs to be made. For the periodized ensemble, the particles are placed in a fixed cell Q_L , and the overlap checks are made not only between the original particles, but also with their periodic translations, see Fig. 2 for an illustration. Following such a protocol with statistical properties properly matching the whole-space counterpart, see Fig. 1(b), gives rise to the *periodized* ensemble and the associated coefficient field A_L^{per} , which is stationary. As will be shown below, the cut particles of A_L^{sn} are considered responsible for deteriorating the quality of the computed homogenized coefficient with respect to the periodized coefficient field A_L^{per} (see eq. (2.9) versus eq. (2.10)).

In either case, we denote by \bar{A}_L the apparent conductivity of A_L on Q_L endowed with periodic boundary conditions, i.e., in analogy to the stochastic setting (2.1), for any $\bar{\xi} \in \mathbb{R}^d$,

$$\bar{A}_L \bar{\xi} = \int_{Q_L} A_L \xi_L dx, \quad (2.4)$$

where $\xi_L \in L^2(Q_L; \mathbb{R}^d)$ solves the equations

$$\xi_L = \bar{\xi} + \Gamma_L \xi_L \quad \text{and} \quad \Gamma_L A_L \xi_L = 0 \quad (2.5)$$

in terms of the Helmholtz projector Γ_L onto gradient fields of periodic functions on the cube Q_L . Notice that the apparent conductivity tensor \bar{A}_L is still a random variable. Also, its expectation $\langle \bar{A}_L \rangle$ will be different from the effective conductivity \bar{A} , in general, which is well-known in the engineering community,

see Huet [36] and Sab [37] for early accounts. However, it can be shown, either in case $A_L = A_L^{\text{sn}}$ [14,15] or in case $A_L = A_L^{\text{per}}$, see Gloria et al. [13] and Clozeau et al. [24] for specific frameworks, that

$$\bar{A}_L \rightarrow \bar{A} \quad \text{as } L \rightarrow \infty \quad (2.6)$$

with probability one, i.e., the apparent conductivity tensors \bar{A}_L approximate the effective conductivity tensor \bar{A} for increasingly large cubes Q_L . In the engineering community, a sufficiently large cell Q_L is called a *representative volume element* [1,3]. Note that boundary conditions different from periodic could be used as well for defining the truncated corrector problem (2.5), e.g., Dirichlet or Neumann boundary conditions, but we chose periodic boundary conditions as they tend to be more accurate for fixed cell size, see, for instance, Kanit et al. [3].

The convergence statement (2.6) is purely qualitative and does not permit to analyze the effect of the size of the volume elements. Indeed, in practice a suitable trade-off between the increased accuracy that accompanies larger computational cells and the limited computational resources needs to be identified, for instance based on statistical estimation techniques [3]. For this purpose, *quantitative convergence statements* become useful. On average, the error may be decomposed in the form

$$\left\langle \|\bar{A}_L - \bar{A}\|^2 \right\rangle = \left\langle \|\bar{A}_L - \langle \bar{A}_L \rangle\|^2 \right\rangle + \|\langle \bar{A}_L \rangle - \bar{A}\|^2 \quad (2.7)$$

in terms of the Frobenius norm, i.e., the right-hand side consists of a random error, which measures the standard deviation of the snapshot ensemble, and a systematic error which quantifies the defect induced by working on a cell of finite size. From a physical point of view, the random error quantifies the lack of statistical representativity of the realization in the finite-sized cell, whereas the systematic error accounts for artificial long-range correlations induced by periodization for A_L^{per} and the boundary-layer error in case of taking snapshots A_L^{sn} .

By using a Monte-Carlo sampling-strategy on cells of fixed size, the random contribution may be decreased - in contrast to the systematic error. Indeed, suppose that N independent coefficient fields $(A_{L,i})$ are sampled. Then, the empirical expectation of the corresponding effective conductivities satisfies

$$\left\langle \left\| \frac{1}{N} \sum_{i=1}^N \bar{A}_{L,i} - \bar{A} \right\|^2 \right\rangle = \frac{1}{N} \left\langle \|\bar{A}_L - \langle \bar{A}_L \rangle\|^2 \right\rangle + \|\langle \bar{A}_L \rangle - \bar{A}\|^2.$$

The decomposition (2.7) is implicit in the statistical approach to estimating the minimum size of a representative volume element pioneered by Kanit et al. [3]. They assume the systematic error, which they call *bias*, to be negligible compared to the random error, which they refer to as *dispersion*.

In general, due to the central limit theorem (CLT), we cannot expect a decay of the random error better than

$$\sqrt{\left\langle \|\bar{A}_L - \langle \bar{A}_L \rangle\|^2 \right\rangle} \lesssim L^{-\frac{d}{2}}. \quad (2.8)$$

This scaling was confirmed by Kanit et al. [3] in computational experiments for synthetic Poisson-Voronoi microstructures and thermal conductivity. In case of elasticity, a slightly inferior scaling was observed.

On the theoretical side, notice that the decay of the error (2.7) may be arbitrarily slow for general stationary and just qualitatively ergodic coefficient fields. Specific quantified ergodicity assumptions permit drawing stronger conclusions. For instance, ensembles with finite range were considered by Armstrong & Smart [38], who provided quantitative stochastic homogenization results for convex integral functionals of quadratic growth. Armstrong & Mourrat [39] relaxed the finite-range assumption and provided results for a mixing condition with algebraic decorrelation rate, previously considered by Yurinskii [40].

As an alternative to the approaches just mentioned, ergodicity may be quantified in terms of suitable functional inequalities in probability [41], which compensate the lack of "natural" Poincaré inequality on

the probability space. Under an L^2 spectral gap assumption, either if A_L is obtained as a snapshot [16, eq. (3.3)] or by periodization [42, Th. 1] [13, Th. 2], the CLT estimate (2.8) is expected to hold. For the latter case, Duerinckx et al. [42, Th. 1] actually identify the first order term in the expansion of $\bar{A}_L^{\text{per}} - \langle \bar{A}_L^{\text{per}} \rangle$. As a consequence, the CLT scaling (2.8) of the random error is indeed optimal.

However, these quantifications of ergodicity only hold under restrictive assumptions on the underlying random coefficient field and may not meet the requirements of practical models of interest to the applied sciences [43]. Thus, spectral gap assumptions allowing for thicker stochastic tails were considered, i.e., in terms of an L^p spectral gap assumption [44] and via a weighted logarithmic Sobolev inequality [45, Def. 1]. Further weighted functional inequalities satisfied by ensembles of relevance to materials science were studied by Duerinckx & Gloria [28, 29].

In contrast to the random error, the convergence rate of the systematic error is sensitive to the way the finite-cell ensemble A_L is build. In general, a boundary-layer error (as introduced earlier) with dimension-independent scaling

$$\|\langle \bar{A}_L^{\text{sn}} \rangle - \bar{A}\| \lesssim L^{-1} \quad (2.9)$$

is expected, see Egloffé et al [16, Eq. (3.4)], and proved to be optimal in Clozeau et al. [24] for a specific class of coefficient fields. If the coefficient fields A_L^{sn} are considered as given, techniques based on modifying the corrector equation (2.5) were proposed [21, 22] to screen the influence of the improperly treated boundary of the considered cell and to restore a better convergence rate. In contrast, using the periodized coefficient field $A_L = A_L^{\text{per}}$ may attenuate the systematic error, so that screening techniques are not necessary.

The latter statement could be made rigorous for specific classes of ensembles that allow for a natural periodization. For i.i.d. discretely random conductivities, Gloria et al. [13, Th. 2] established the estimate

$$\|\langle \bar{A}_L^{\text{per}} \rangle - \bar{A}\| \lesssim L^{-d} \quad (2.10)$$

for $d > 2$, where there is an additional factor of $\ln^d(L)$ in the r.h.s. Such a result is known to hold for the case of overlapping Poisson random inclusions. For the case where the ensemble is generated from a Gaussian field with integrable covariance function, Clozeau et al. [24] showed estimate (2.10), and proved this scaling to be optimal in this setting by identifying the first order term of the asymptotic expansion of $\langle \bar{A}_L^{\text{per}} \rangle - \bar{A}$.

3 Computational tools

In this Section we provide details on the microstructure-generation methods used as the basis for the computational experiments conducted in Section 4.

3.1 The mechanical contraction method

In this Section we describe the mechanical-contraction method (MCM) of Williams-Philipse [32] used for generating circle packings (in 2D) and sphere packings (in 3D). For composites with spherical fillers, the simple random sequential adsorption algorithm of Feder [46] is unable to reach industrial-scale volume fractions in reasonable time. Indeed, the jamming limit of mono-sized spheres is approximately 38% [47], which is insufficient for the computational experiments of Section 4.1 below, taking into account the isolation distance.

For this purpose, collective rearrangement algorithms are necessary, and several methods are available [48, 49]. We shall describe the mechanical-contraction method, as there is a modification which generalizes to cylindrical fillers.

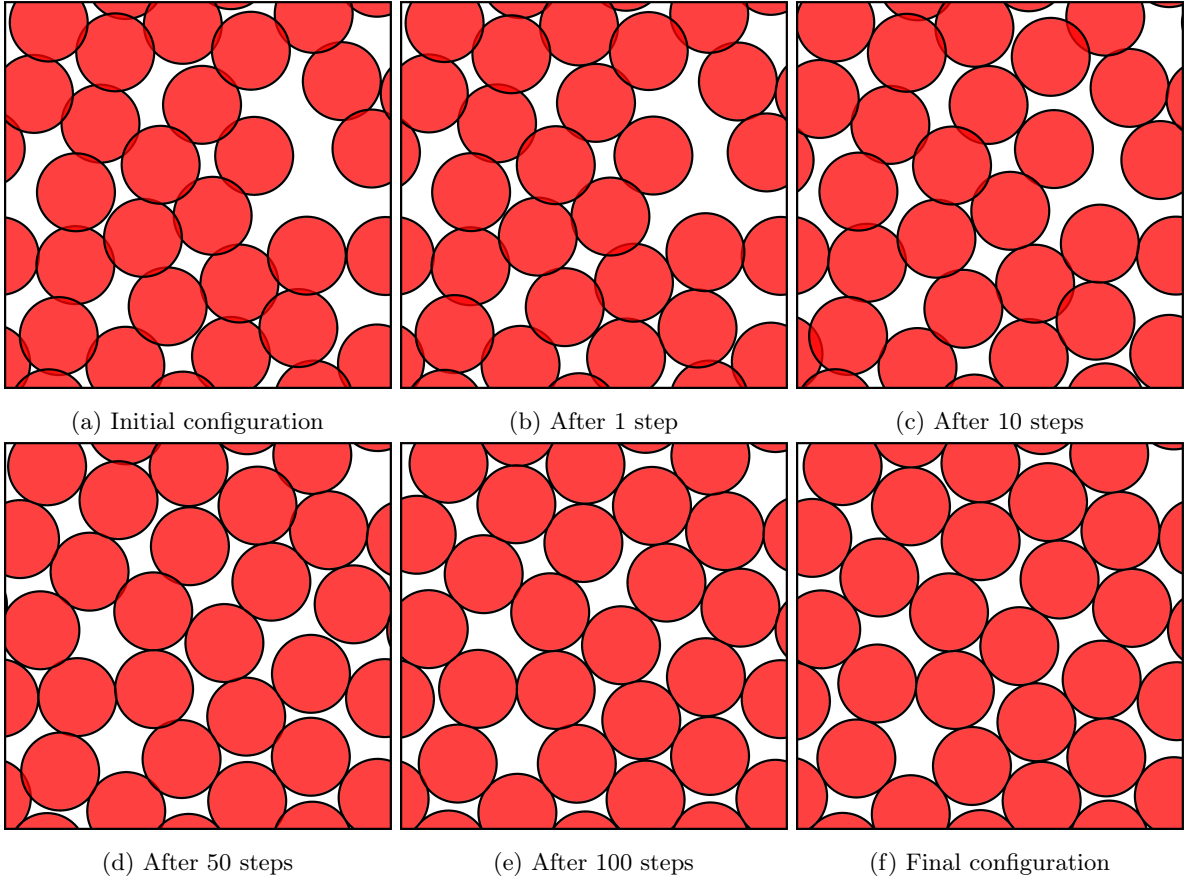


Figure 3: Illustration of the overlap-removal technique central to the mechanical contraction method [32], applied to 25 circles and an area fraction of 80%

Suppose that a radius r and a cubic cell Q_L are given, together with an initial distribution of midpoints x_1, \dots, x_N , each contained in Q_L . Suppose that r , L and N are chosen in such a way that, if all spheres centered at the midpoints are non-overlapping, the target volume fraction ϕ would be reached. If the spheres are overlapping, the MCM applies an overlap-removal technique in order to move the midpoints x_1, \dots, x_N in such a way that the spheres do not overlap anymore. For this purpose, an overlap energy

$$W : Q_L^N \rightarrow \mathbb{R}, \quad (x_1, \dots, x_N) \mapsto \frac{1}{2} \sum_{1 \leq i < j \leq N} \delta(x_i, x_j)^2, \quad (3.1)$$

is defined in terms of an overlap indicator

$$\delta(x_i, x_j) = \langle 2r - \text{dist}(x_i, x_j) \rangle_+, \quad (3.2)$$

where $\text{dist}(x_i, x_j)$ denotes the Q_L -periodic distance of x_i and x_j and

$$\langle z \rangle_+ = \max(0, z)$$

is the Macauley bracket. Two (open) spheres with radius r centered at x_i and x_j , respectively, do not overlap if and only if $\delta(x_i, x_j) = 0$. Thus, the N spheres centered at x_1, \dots, x_N are in a non-overlapping configuration precisely if $W(x_1, \dots, x_N) = 0$. As the overlap energy W (3.1) is continuously differentiable, a gradient-descent method may be used for finding a global minimizer of W , see Williams-Philipse [32] for details. The approach is illustrated in Fig. 3, where 25 disks were placed in an initially random

configuration at 80% volume fraction. During the iterations, the centers of overlapping disks are moved, whereas disks without overlap remain fixed. For this example, the overlap-removal algorithm converged to the desired precision after 288 iterations.

In the MCM algorithm, an increasing sequence of volume fractions $\phi_1, \phi_2, \dots, \phi_K$ is defined. For the initial volume fraction ϕ_1 (which is typically rather low), the initial centers of the spheres are drawn from a uniform distribution on the corresponding cube. Then, the overlap-removal technique is applied. Once a non-overlapping configuration is reached for ϕ_k , both the cell and the sphere centers are rescaled in such a way that the non-overlapping configuration would have a volume fraction ϕ_{k+1} . Then, the overlap-removal technique is applied. The process is repeated until the desired volume fraction ϕ_K is reached. The repeated shrinking is responsible for the name of the algorithm: mechanical contraction method. Several remarks are in order.

1. The complexity of the MCM algorithm is hidden in computing the pairwise distances (3.2). A naive implementation requires on the order of N^2 computations, which can be excessive for large N . We rely upon cell-linked lists [50] to reduce the complexity to $O(N)$.
2. In practice, an isolation distance between the spheres is useful to avoid singularities in the solution field. This is realized by working with a slightly larger radius $\tilde{r} > r$ when computing the overlap indicator (3.2).

3.2 Sequential addition and migration

The mechanical contraction method of Williams-Philipse [32] also applies to spherocylinders, i.e., cylinders with spherical caps attached, provided the overlap indicator (3.2) is modified. A microstructure generated in this way may be used as a model of a fiber-reinforced composite by neglecting the spherical caps of the spherocylinders.

In its original form, however, the method can only generate moderate volume fractions without altering the overall fiber orientation. For this reason, Schneider [33] modified the overlap energy W (3.1) by a penalty term accounting for the orientation. Also, in order to reach higher volume fractions, instead of successively shrinking the cell, fibers are added incrementally to a cell of fixed size. The resulting algorithm is called sequential addition and migration (SAM), see Schneider [33] for details.

4 Computational results

4.1 Setup

We are concerned with microstructures of particle-reinforced composites. We used the isotropic thermal conductivity of polypropylene ($0.2\text{W}/(\text{m}\cdot\text{K})$) for the matrix and of E-glass ($1.2\text{W}/(\text{m}\cdot\text{K})$) for the fillers, see Dorn-Schneider [51].

The microstructures were discretized on a regular pixel/voxel grid, segmented according to which phase the midpoint of the pixel/voxel belongs to. The static thermal equilibrium problem (2.5) was discretized by the Moulinec-Suquet discretization [30, 31], an underintegrated Fourier-Galerkin discretization [52], see Brisard-Dormieux [53] and Schneider [54] for convergence proofs. For resolving the discrete system, we used the Eyre-Milton solver [55], a Douglas-Rachford type solution method [56], with a tolerance of 10^{-6} , implemented in Python with Cython extensions, see Schneider [57] for more details.

For the circular and spherical inclusions, a desktop computer with a 6-core Intel i7 CPU and 32GB

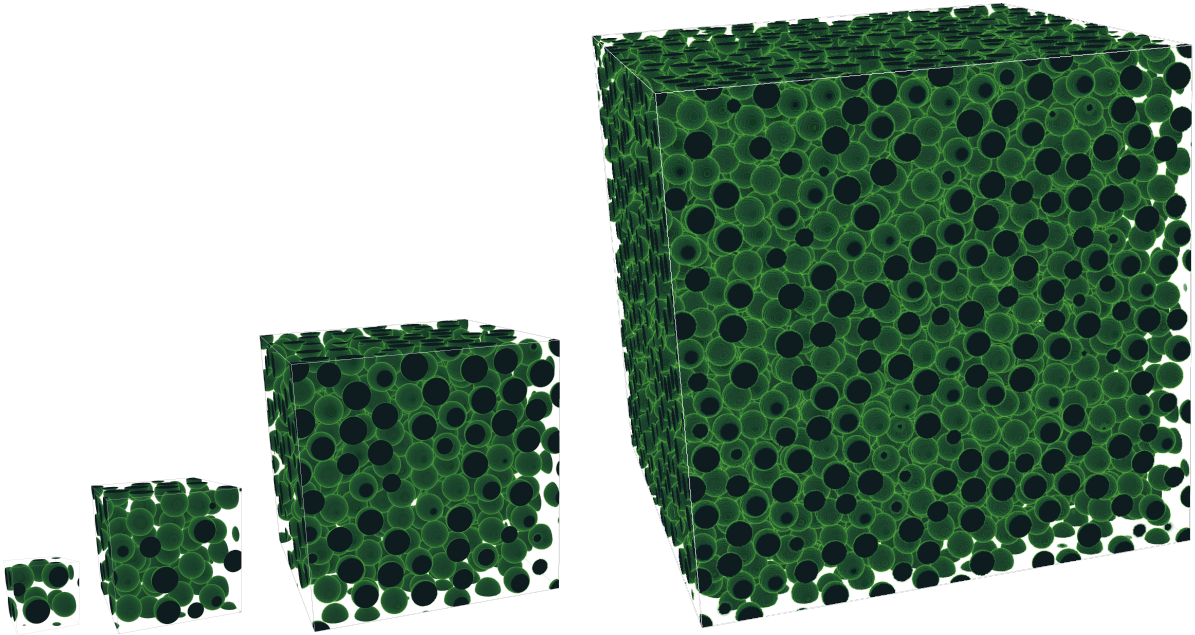


Figure 4: 3D comparison of periodically generated cells and increasing number of inclusions, with $2^3 = 8$, $4^3 = 64$, $8^3 = 512$ and $16^3 = 4096$ spheres (from left to right)

RAM was utilized. A dual-socket workstation with 48 cores and 1 TB RAM was used for the short-fiber microstructures.

4.2 Spherical inclusions

We investigate mono-disperse spherical fillers as our first example. For generating microstructures, we follow two protocols. The first strategy, which we call *periodized*, generates K^3 ($K = 2, 4, 8, 16$) non-overlapping spheres by the mechanical contraction method, see Section 3.1. For the second, *snapshot* strategy, $(2K)^3$ non-overlapping spheres are packed as before, but we cut out 1/8th of the structure. Thus, we arrive at a non-periodic structure of identical size as for the previous protocol.

For both approaches, we fill to 30% by the mechanical contraction method of Williams and Philippse [32] in 10% steps, and we use an isolation distance of 20% of the sphere's radius.

A unit cell containing K^3 spheres (on average) is discretized by $(16K)^3$ voxels, i.e., the microstructures for $K = 16$ are discretized by $256^3 = 16\,777\,216$ elements and contain 4096 spheres. Following Khoromskaia et al. [26], Section 5, we generated 10000 microstructures for $K = 2, 4, 8, 16$ and the two protocols. The most time-consuming step here was generating the snapshot elements with $K = 16$, because 10000 volume elements, each containing 32768 non-overlapping spheres, needed to be generated quickly.

For each of the 10000 generated microstructures, we computed the 11-component of the effective thermal conductivity. To keep notation simple, we introduce

$$\bar{a} = \bar{A}_{11} \quad (4.1)$$

as our quantity of interest. In contrast to the volume fraction, the ground truth for \bar{a} is not known exactly. For that reason, we need to resort to computations on a suitable large scale. More precisely, we generated ten large microstructures with the periodization strategy, see Fig. 5, with $64^3 = 262\,144$ spherical inclusions, discretized by $1024^3 \approx 1.07 \times 10^9$ voxels, and computed the reference

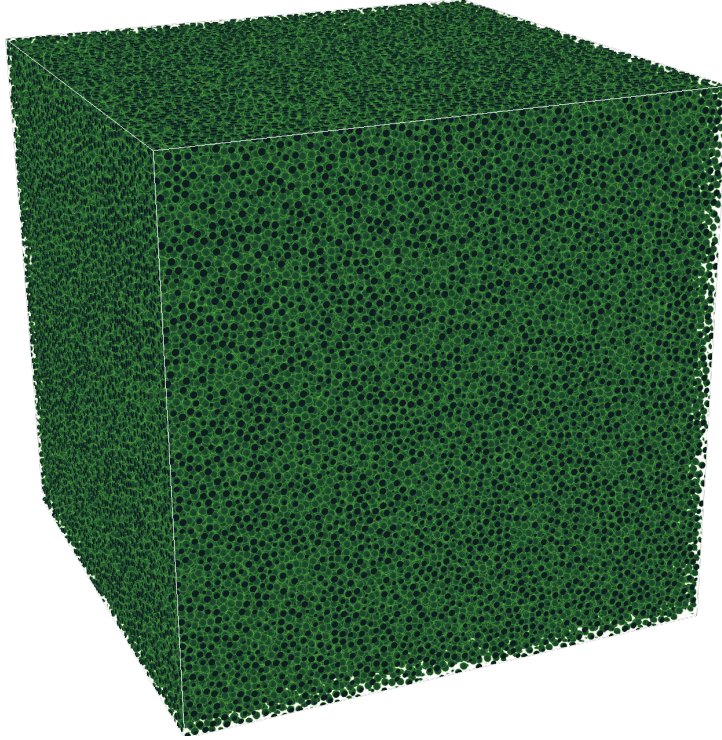


Figure 5: A large volume element with $K = 64$, i.e., $64^3 = 262\,144$ spheres used for computing the reference effective conductivity (4.2)

$$\bar{a} = 0.345228 \pm 0.000015 \text{ W}/(\text{m}\cdot\text{K}). \quad (4.2)$$

Here, Student's t -distribution for $t = 10$ is used for estimating a 99% two-sided confidence interval based on the (-1) -shifted standard deviation computed for these ten samples. Tab. 1 contains the computed

K	periodized	snapshots	K	periodized	snapshots
2	$0.345553 \pm 5[-5]$	$0.356449 \pm 4[-4]$	2	0.0017786	0.0172593
4	$0.345538 \pm 2[-5]$	$0.351227 \pm 2[-4]$	4	0.0006614	0.0080232
8	$0.345382 \pm 6[-6]$	$0.348215 \pm 1[-4]$	8	0.0002450	0.0043529
16	$0.345291 \pm 2[-6]$	$0.346698 \pm 5[-5]$	16	0.0000871	0.0020374
64	$0.345224 \pm 1[-5]$	–	64	0.0000107	–

Table 1: Computed effective conductivities \bar{a}_L (left) and standard deviations (right) in $\text{W}/(\text{m}\cdot\text{K})$ for the spheres, computed using 10 000 realizations

means and standard deviations for $K = 2, 4, 8, 16$ and the periodized/snapshot protocols. The mean values are supplemented by 99%-two sided confidence intervals, computed using the standard deviations, and rounded to the highest significant digit. Due to the large number of samples used, these confidence intervals are much tighter for $8 \leq K \leq 16$ than for the ten computations on large volume elements, cf. Fig. 5. The systematic error for the periodized ensembles is about an order of magnitude smaller than for their snapshot counterparts, cf. Fig. 6(a). For the latter, an L^{-1} -convergence behavior is evident. However, from an engineering point of view, a systematic error below 0.1% is sufficient - and this is computed using only 8 (!) inclusions.

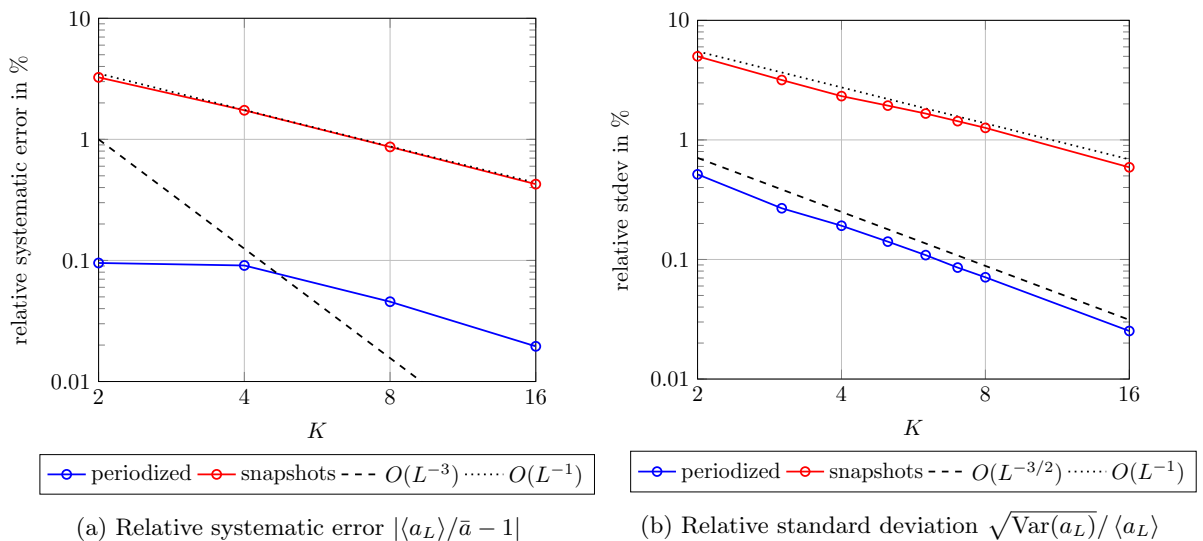


Figure 6: Convergence behavior of the systematic and the random error for spherical inclusions and the periodized/snapshot protocols, normalized according to equation (4.2)

K	periodized	snapshots	K	periodized	snapshots
2	95.77	12.20	2	17.36	1.42
4	100.00	24.06	4	35.29	2.35
8	100.00	45.45	8	76.06	4.68
16	100.00	82.73	16	99.93	10.13

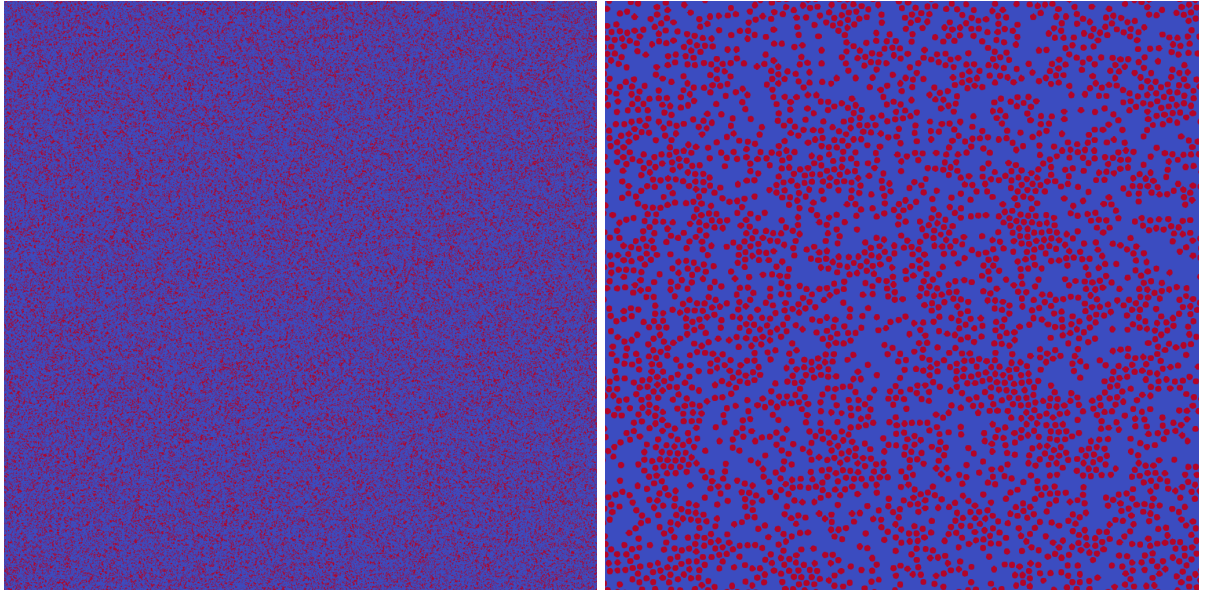
Table 2: Empirical probability (in %, 10 000 realizations) of being 1%-close (left) and 0.1%-close (right) to \bar{a} (4.2) for spherical fillers and 30% volume fraction

Taking a look at the relative standard deviation, cf. Fig. 6(b), we observe that the snapshot-sampling strategy leads to a convergence rate of $1/L$. In contrast, the standard deviation for the periodized ensemble decreases as $L^{-3/2}$. Also, there is a difference by an order of magnitude difference between the two protocols.

Due to proper scaling of the systematic and random errors in Fig. 6, we may also quantify the uncertainty involved in the computation. Indeed, the random error is about an order of magnitude larger than the systematic error for both protocols.

Mean and standard deviations only provide a limited amount of information concerning the full distribution of the random variable a_L . For this purpose, and from an engineering perspective, we may ask the following question: Suppose we run only a single computation, what is the probability of being 1% (0.1%) close to the reference (4.2)? Using the 10 000 computations for each setup, the empirical probabilities are collected in Tab. 2. We see that, for the periodized protocol, more than two correct digits are computed with a chance of more than 95% using $2^3 = 8$ spheres. For higher K , each of the 10 000 computations predicted two significant digits correctly. In contrast, for the snapshot protocol, even using $16^3 = 4096$ spheres led to a lower success probability than for eight spheres in the periodized setting.

Computing the third significant digit with a single run is more challenging, and $K \geq 8$ is required for the periodized protocol to have a higher success than failure probability. Only for $K = 16$, i.e., 4096 spheres, three significant digits may be computed almost surely. Indeed, only 7 out of 10 000 runs failed



(a) Total view ($16\,384^2$ pixels)

(b) Cut-out of $(1/16) \times (1/16)$ th ($1\,024^2$ pixels)

Figure 7: First of the ten microstructures with $1\,024^2$ disks used for computing the effective conductivity (4.3)

to provide three significant digits.

In contrast, for the snapshot approach, the success probability is about an order of magnitude smaller.

4.3 Circular inclusions

Subsequent to studying spherical inclusions, we turn to circular inclusions in two spatial dimensions. Microstructures of this type serve as models for continuous fibers, i.e., parallel cylindrical inclusions whose length is much larger than the diameter, and the effective behavior may be determined from a two-dimensional model. In turn, we may investigate the changes in convergence rates for stochastic homogenization when decreasing the ambient dimension.

We followed a similar protocol as for the spherical case, with the notable difference that we only need to cut out $1/4$ th from a sample containing $(2K)^2$ disks to obtain the snapshot. To ensure some degree of compatibility, we retained the area-fraction steps and the isolation distance for the MCM algorithm. We also used $(16K)^2$ pixels for discretizing the geometries filled by K^2 disks, on average. Due to the two-dimensional situation, we were able to treat larger K than for the three-dimensional case. For reference, we generated ten microstructures with a periodized protocol with $1\,024^2 = 1\,048\,576$ circular inclusions, see Fig. 7, discretized by $16\,384^2$ pixels. We obtained a reference conductivity, measured transverse to the fibers, of

$$\bar{a} = 0.3174257 \pm 0.0000214 \text{ W}/(\text{m}\cdot\text{K}), \quad (4.3)$$

including a two-sided 99%-confidence interval based on Student's t -distribution for the ten drawn samples, and using identical material parameters as for the spherical inclusions. Notice that the effective conductivity (4.3) transverse to continuous fibers is smaller than the effective conductivity of spherical fillers (4.2) at the same filler fraction.

To assess the convergence behavior of the transverse effective conductivity, we generated 10 000 microstructures for K ranging from 2 to 64 in dyadic steps, both for the periodized and the snapshot

K	periodized	snapshots	K	periodized	snapshots
2	$0.316286 \pm 2[-4]$	$0.324902 \pm 1[-3]$	2	0.007254	0.045318
4	$0.317640 \pm 1[-4]$	$0.320024 \pm 7[-4]$	4	0.004890	0.026951
8	$0.317517 \pm 6[-5]$	$0.318881 \pm 4[-4]$	8	0.002419	0.014757
16	$0.317505 \pm 3[-5]$	$0.318172 \pm 2[-4]$	16	0.001181	0.007808
32	$0.317459 \pm 2[-5]$	$0.317617 \pm 1[-4]$	32	0.000592	0.004039
64	$0.317438 \pm 7[-6]$	$0.317591 \pm 5[-5]$	64	0.000291	0.002059
1024	$0.317426 \pm 2[-5]$	–	1024	0.000021	–

Table 3: Computed effective conductivities \bar{a}_L (left) and standard deviations (right) in $W/(m \cdot K)$ for the circular inclusions, computed using 10 000 realizations

protocol, and computed the \bar{a} -value. The results are collected in Tab. 3, together with the estimated standard deviations. For comparison, also the computed value for $K = 1024$ was included. As for the spherical case, the confidence interval for the $K = 1024$ reference computation is comparatively large, approximately identical to the $K = 32$ case. This effect is a consequence of using 10 samples for $K = 1024$ instead of 10 000 samples for $K = 32$. Also notice that $K = 64$ corresponds to $K^2 = 4096$ circular inclusions, discretized on a regular grid with 1024^2 pixels. We observe, see Fig. 8(a), that the systematic

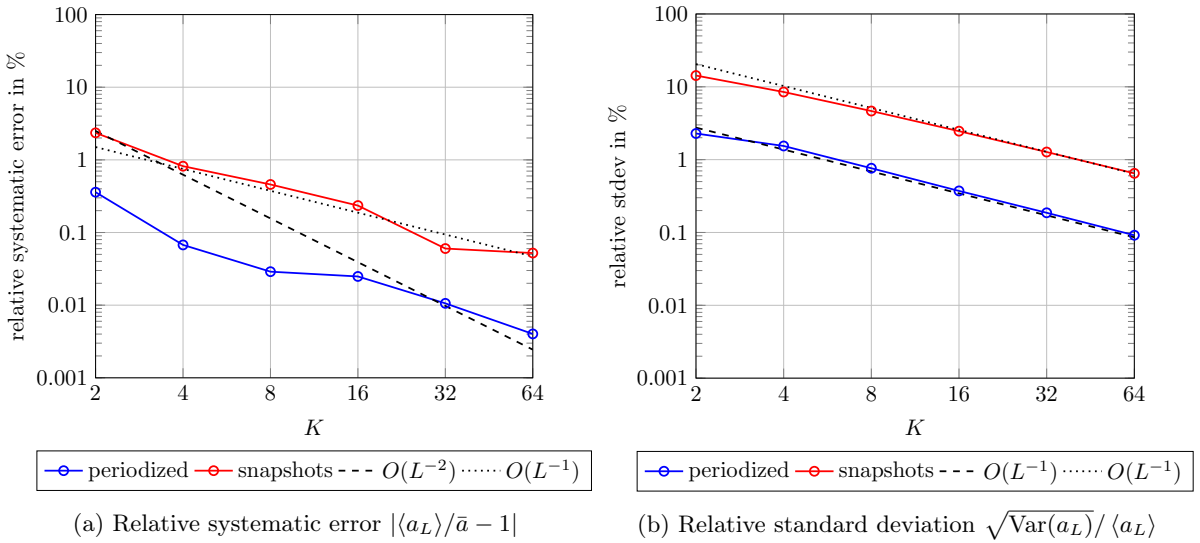


Figure 8: Convergence behavior of the systematic and the random error for circular inclusions and the periodized/snapshot protocols, normalized according to equation (4.3)

error of the periodized protocol is consistently smaller than for the snapshot approach, almost by an order of magnitude. For the snapshot ensemble, the systematic error follows an $1/L$ -rate, as predicted. Evaluating the periodized protocol is much more difficult, as the systematic error is extremely small. In particular, and in view of the confidence interval of the reference computation, see Tab. 3, we cannot safely provide a convergence rate. For the standard deviation, see Fig. 8(b), both protocols lead to an $1/L$ -convergence rate. Thus, in contrast to the spherical case, there is no difference in convergence rates between the periodized and the snapshot ensemble. We will discuss the reasons behind this effect in Section 5. The standard deviation for the snapshot approach is about an order of magnitude larger than for the periodized setting. Comparing the levels of stochastic and systematic error, see 8, for both

K	periodized	snapshots	K	periodized	snapshots
2	32.35	5.61	2	3.47	0.67
4	50.27	9.47	4	5.47	0.92
8	80.93	17.52	8	10.81	1.78
16	99.25	30.95	16	21.30	3.24
32	100.00	56.77	32	40.60	5.86
64	100.00	87.47	64	72.71	12.31

Table 4: Empirical probability (in %, 10 000 realizations) of being 1%-close (left) and 0.1%-close (right) to \bar{a} (4.3) for circular inclusions

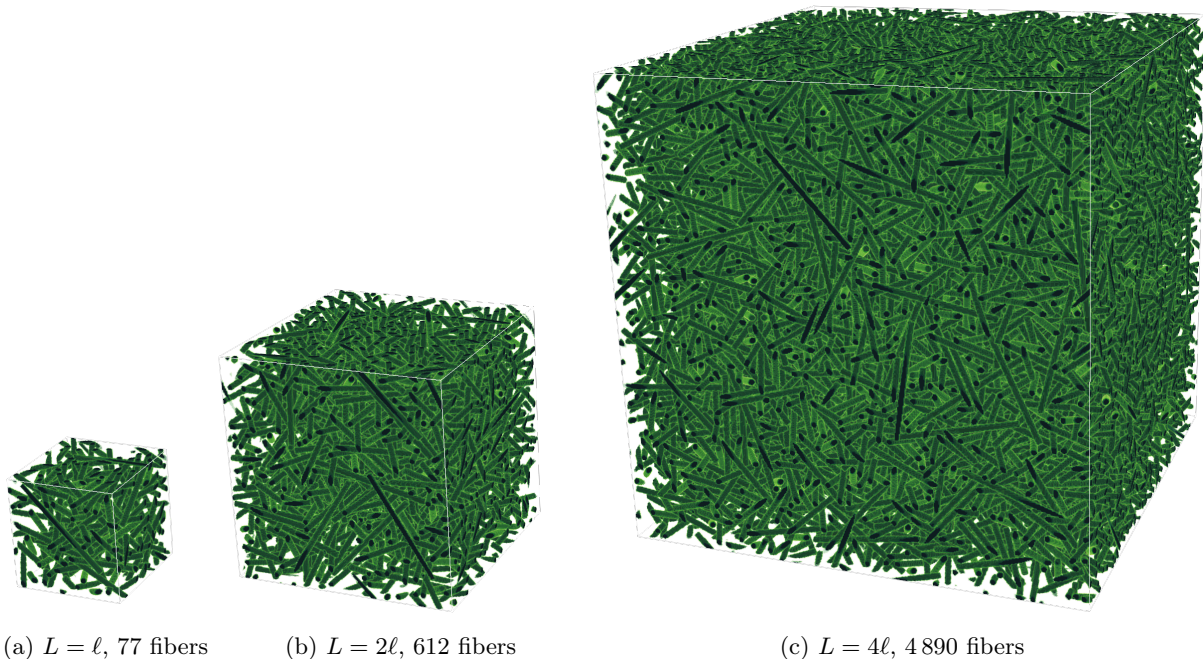


Figure 9: Periodically generated short-fiber reinforced elements with increasing fiber count

approaches the random error is about an order of magnitude larger than the systematic error.

As for the spherical inclusions treated in Section 4.2, we take a look at the empirical success probabilities of obtaining two and three, respectively, significant digits with only a single computation, see Tab. 4. For the periodized protocol, 16^2 circular inclusions are required to obtain two correct digits with 99% probability, i.e., more than 100 fibers are required. In contrast, for the snapshot strategy, $32^2 = 1024$ inclusions are required to exceed 50% success probability, a value that is exceeded for $4^2 = 16$ inclusions in case of the periodized protocol.

Obtaining three correct significant digits is difficult in the two-dimensional setting, even for the periodized protocol. Indeed, even working with $64^2 = 4096$ inclusions leads to a failure rate of about 30%.

4.4 Short-fiber reinforced composites

Last but not least, we consider short-fiber reinforced composites, i.e., microstructures consisting of non-overlapping cylindrical inclusions. More precisely, we consider identically shaped cylindrical fibers with length ℓ and diameter d at an aspect ratio ℓ/d of 20, with an isotropic fiber orientation, encoded by an

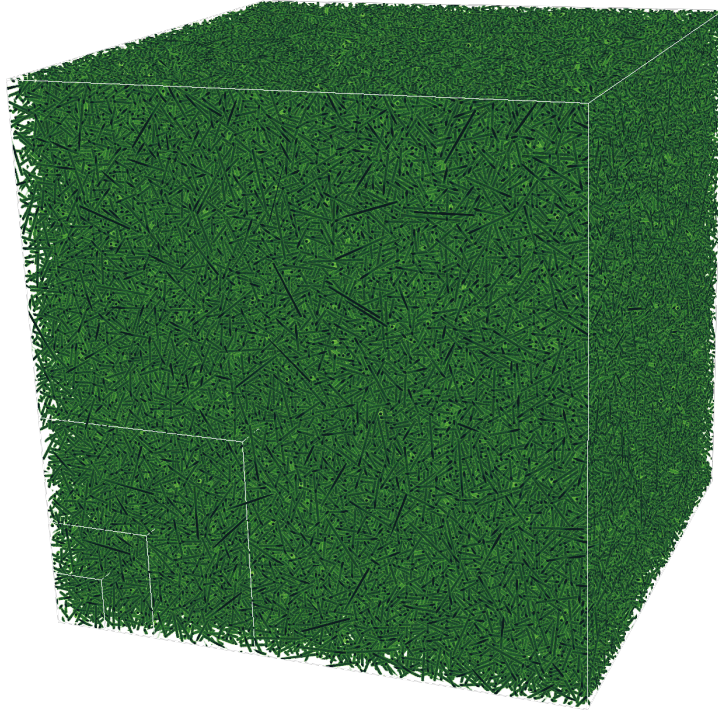


Figure 10: Large volume element with $L/\ell = 10$, including 76 397 fibers. Smaller cell sizes with $L/\ell \in \{1, 2, 4\}$ are indicated by white boxes in the lower left corner

isotropic fourth-order fiber-orientation tensor [58].

We shall also consider a periodized and a snapshot protocol. In the periodized setting, we fill to 15% volume in three 5%-steps by Sequential Addition and Migration [33], see Section 3.2, with a minimum distance of 20% of the fiber's diameter, and consider cubic volume elements Q_L , s.t. the edge length L is an integer multiple of the fiber length ℓ , i.e., $L/\ell = 1, 2, 3, 4$, see Fig. 9 for examples.

For the snapshot protocol, we generate cells $Q_{\frac{3}{2}L}$ with the periodic protocol und extract a subcell of dimension L^3 . As in the previous two Sections, we endow the matrix with the (isotropic) conductivity parameters of PP ($0.2\text{W}/(\text{m}\cdot\text{K})$) and the fibers with those of E-glass ($1.2\text{W}/(\text{m}\cdot\text{K})$). Each fiber is discretized by 5 voxels per diameter [59], i.e., 100 voxels per length ℓ . This translates into $(L/\ell \times 100)^3$ voxels in total, i.e., 100^3 voxels for $L = \ell$ and 400^3 voxels for $L = 4\ell$.

We use the average of 10 computed effective conductivities for samples with $L/\ell = 10$ ($1\,000^3$ voxels, see Fig. 10) as the reference:

$$\bar{a} = 0.281008 \pm 0.0000055 \text{ W}/(\text{m}\cdot\text{K}), \quad (4.4)$$

including a 99% two-sided confidence interval, as before. The empirical means of 10 000 computed effective conductivities for the considered volume-element sizes and the two protocols are listed in Tab. 5, together with two-sided 99% confidence intervals and standard deviations. For completeness, the reference data (4.4) are also included.

Notice that the confidence intervals are very tight in this setting. Indeed, due to the shape of the inclusions, even for $L = \ell$, twenty fiber diameters fit across an edge of such a volume element. In fact, the confidence interval for $L = \ell$ is very close to the confidence interval for $L = 10\ell$, as 10 000 samples were evaluated for the former, and only ten samples for the latter. Even for the snapshot-sampling strategy the random errors are small. This accuracy is also reflected in the normalized systematic and random

$\frac{L}{\ell}$	periodized	snapshots	$\frac{L}{\ell}$	periodized	snapshots
1	$0.281079 \pm 6[-6]$	$0.280321 \pm 1[-4]$	1	0.000223	0.003678
2	$0.281211 \pm 2[-6]$	$0.280583 \pm 5[-5]$	2	0.000087	0.001823
3	$0.281060 \pm 1[-6]$	$0.280716 \pm 3[-5]$	3	0.000047	0.001178
4	$0.281042 \pm 1[-6]$	$0.280766 \pm 2[-5]$	4	0.000031	0.000837
10	$0.281008 \pm 6[-6]$	–	10	0.000006	–

Table 5: Computed effective conductivities \bar{a}_L (left) and standard deviations (right) in W/(m·K) for short fibers, computed using 10 000 realizations

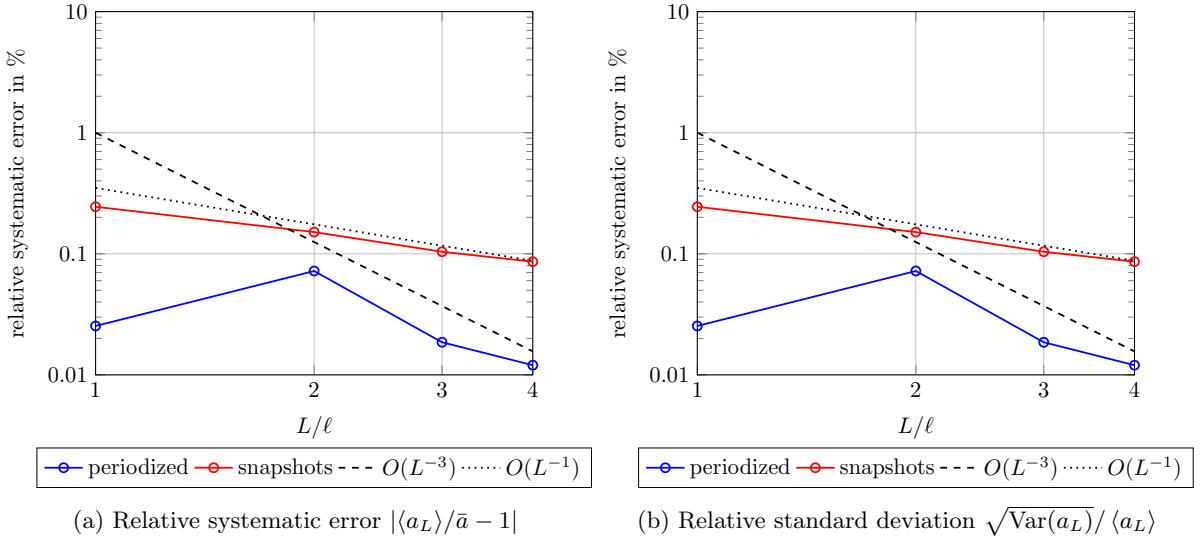


Figure 11: Convergence behavior of the systematic and the random error for short fibers and the periodized/snapshot protocols, normalized according to equation (4.4)

errors, see Fig. 11(b). For all settings considered, they do not exceed 2%.

For the systematic error, see Fig. 11(a), the snapshot strategy shows the already familiar $1/L$ -scaling, whereas the periodized sampling protocol appears to scale as L^{-3} for $L \geq 2\ell$. Between $L = \ell$ and $L = 3\ell$, the systematic error does not decrease monotonically, presumably due to a geometric influence. Indeed, for $L = \ell$, an edge of the volume element under consideration is exactly equal to a fiber length. The comparatively low systematic error for this case may thus be a result of the severe restrictions in fiber arrangement for $L = \ell$. In magnitude, the systematic error for the snapshot approach is about half an order of magnitude larger than for the periodized sampling.

For the random error, see Fig. 11(b), we observe an L^{-1} and $L^{-\frac{3}{2}}$ scaling for the snapshot and periodized protocol, respectively, in agreement with the observations made for spheres, see Fig. 6. Also, there is about an order of magnitude difference in the absolute standard deviations for both approaches, already evident in Tab. 5. It is interesting to note that, for the periodized sampling, the random error is on the same order of magnitude as the systematic error. This behavior contrasts what we observed for spherical and circular inclusions.

As for the other inclusion types, the empirical probabilities for remaining within 1% (and 0.1%) relative error for only a single computation are given in Tab. 6. For the periodized sampling strategy, each of the 40 000 computation was correct to two significant digits. Also, the chance for obtaining three correct

$\frac{L}{\ell}$	periodized	snapshots	$\frac{L}{\ell}$	periodized	snapshots
1	100.00	55.09	1	77.12	6.14
2	100.00	86.54	2	81.91	11.63
3	100.00	98.02	3	100.00	17.85
4	100.00	99.91	4	100.00	24.59

Table 6: Empirical probability (in %, 10 000 realizations) of being 1%-close (left) and 0.1%-close (right) to \bar{a} (4.2) for fibers

digits exceeds $3/4$ for $L = \ell$, already. For $L = 3\ell$ and above, each individual computation was guaranteed to feature three correct digits. In contrast, for the snapshot sampling, the success probabilities are much smaller. An edge length $L = 3\ell$ is required to obtain two correct digits with 98% probability, and the involved effort is at least $3^3 = 27$ times as high as using an element from the periodized ensemble and $L = \ell$. Obtaining higher accuracy than two digits appears out of reach for the snapshot strategy. Even for $L = 4\ell$, only a quarter of the 10 000 computations led to results with three correct leading digits.

5 On the non-standard scaling of the random error in three dimensions

This section is intended to complement the results of the previous section. More precisely, we provide insights into the difference in the decay behavior of the random error for the snapshot ensembles compared to their periodized counterparts. It will also become clear why we observe this behavior in three spatial dimensions only.

For a random conducting medium with two distinct (positive) conductivities α_1 and α_2 , a series expansion in terms of the material-contrast related quantity

$$\rho = \frac{\sqrt{\alpha_1} - \sqrt{\alpha_2}}{\sqrt{\alpha_1} + \sqrt{\alpha_2}}$$

permits identifying the leading-order term in the estimate

$$\sqrt{\langle \|\bar{A} - \bar{A}_L\|^2 \rangle} \leq 4\sqrt{\alpha_1\alpha_2}\sqrt{\text{Var}(\phi_L)}\rho + O(\rho^2). \quad (5.1)$$

We refer to Appendix A for a self-contained derivation. Thus, the decay rate of the random error is closely tied to the decay rate of the variance of the sampled volume fraction. In Fig. 12(a), we compare the standard deviations of the volume fractions ϕ_L for the periodized and the snapshot protocol and spherical fillers. As the number of inclusions is fixed to K^3 for the periodized ensemble, the volume fractions are exact up to voxelation, i.e., the rastering process which furnishes each voxel either by matrix or filler material. The latter process, as it is based on the voxel's centroid, shows a $L^{-3/2}$ -scaling in accordance with the CLT. For the snapshot ensemble, however, we observe an L^{-1} -scaling. In addition, we also sampled the number of spherical inclusions from a Poisson process, and used the MCM to generate a corresponding periodized Poisson ensemble. Unfortunately, if K was too small, the number of cells produced by the Poisson process often led to a filler content that could not be realized by MCM. For that reason, only results for $K \geq 4$ are shown. Fig. 12(a) shows an $L^{-3/2}$ -decay of the standard deviation for the periodized Poisson process. However, the absolute values are on a higher level than for the previously discussed protocols. Please note that the mean volume fractions for all three considered scenarios and all

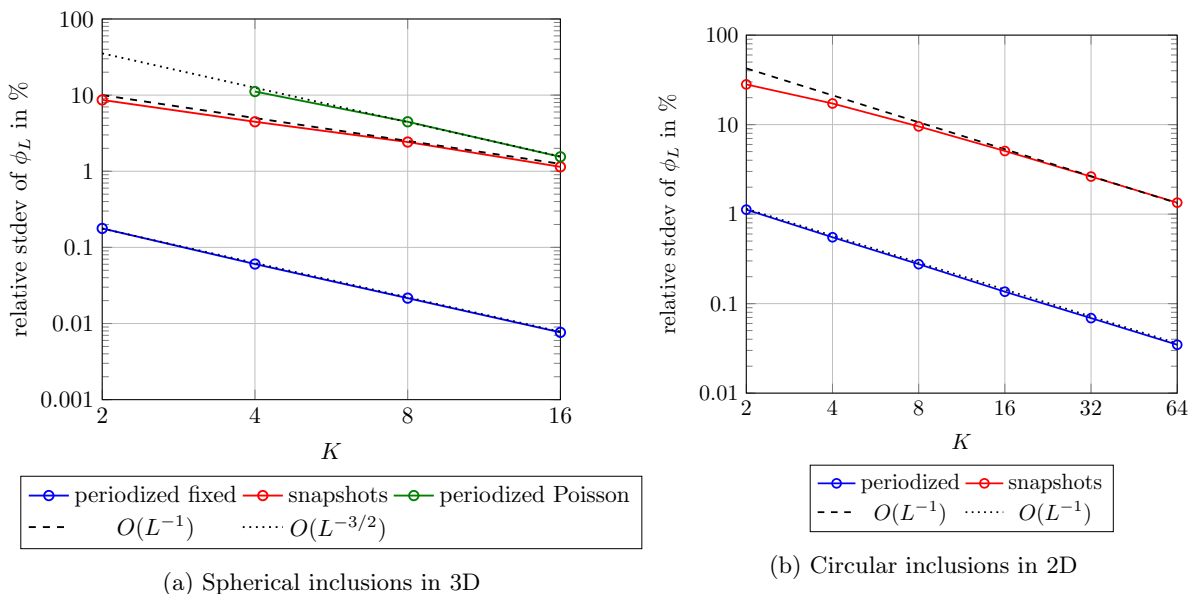


Figure 12: Convergence behavior of the standard deviation for computing the volume fraction ϕ_L and periodized/snapshot protocols

considered K were within 0.1% relative error of the target 30% volume fraction.

For comparison, the decay rates of the sampled volume fractions of the circular inclusions are shown in Fig. 12(b). Both the periodized and the snapshot-sampling strategies are characterized by a $1/L$ -scaling, in accordance with the CLT.

As an intermediate result, we conclude that the non-standard scaling of the random error, which we observed in Section 4, is already present at the level of the volume fraction. Fortunately, understanding the sampling of the volume fraction is simpler than understanding the random error through homogenization. Indeed, there is a (more) direct link between the autocorrelation function and the decay behavior of the volume fraction for the snapshot protocol, which arises as the mean of the (random) characteristic-function snapshot on cells Q_L of finite size.

For estimating the decay rate of the volume fraction for snapshot ensembles, the notion of integral range [60, 61] is very useful, and we will quickly summarize the important points.

Suppose that Z is a stationary random field on \mathbb{R}^d with finite second moment. By stationarity, the mean

$$\mu = \langle Z(x) \rangle \quad \text{and the variance} \quad \sigma^2 = \text{Var}(Z(x)) \equiv \langle (Z(x) - \mu)^2 \rangle$$

are independent of $x \in \mathbb{R}^d$. For any compact set $V \subseteq \mathbb{R}^d$, let us denote by Z_V the random variable obtained by averaging Z over V

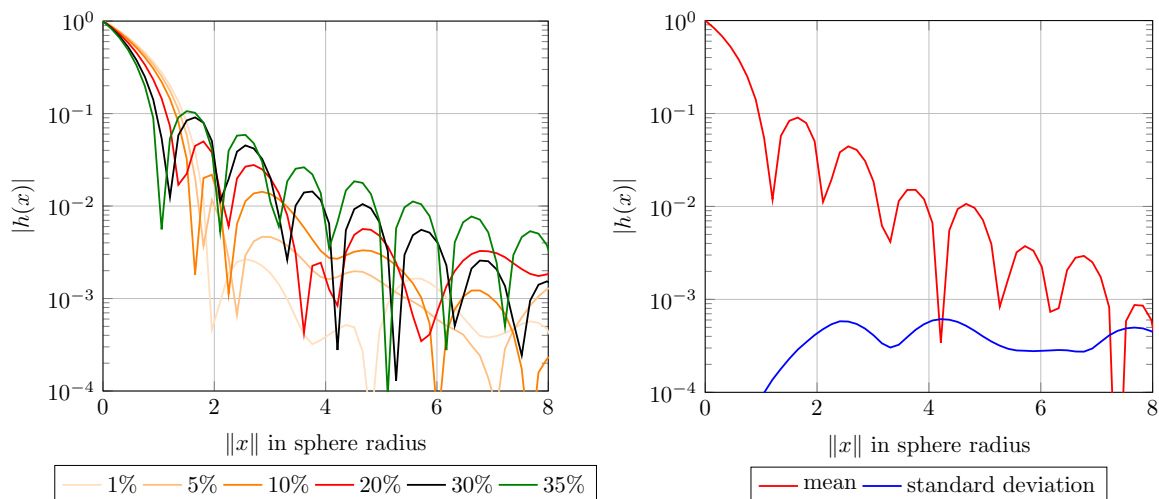
$$Z_V = \int_V Z(x) dx.$$

Z_V gives rise to an unbiased estimator for the mean μ . For $\sigma > 0$, we are interested in the variance of Z_V ,

$$\text{Var}(Z_V) = \left\langle \left(\int_V Z(x) dx - \mu \right)^2 \right\rangle \equiv \sigma^2 \int_V \int_V h(x-y) dx dy, \quad (5.2)$$

expressed in terms of the scaled autocorrelation function

$$h(x) = \sigma^{-2} \langle (Z(0) - \mu)(Z(x) - \mu) \rangle. \quad (5.3)$$



(a) Single realizations at $L/\ell = 32$ and varying fiber volume content ϕ (b) Mean and standard deviation for ten realizations at $L/\ell = 64$ and $\phi = 30\%$

Figure 13: Magnitude of the autocorrelation function $|h|$, depending on $\|x\|$

The identity (5.2) uncovers the relation between the variance of the V -averaged variable Z_V and the autocorrelation function (5.3). If $h \in L^1$, the estimate

$$\text{Var}(Z_V) \leq \sigma^2 \int_V \int_V |h(x-y)| dx dy \leq \frac{\sigma^2}{|V|} \int_V \int_{\mathbb{R}^d} |h(x-y)| dx dy = \frac{\sigma^2 \|h\|_{L^1}}{|V|},$$

holds, i.e., when evaluated on the cube $V = Q_L$,

$$\text{Var}(Z_{Q_L}) \leq \sigma^2 \|h\|_{L^1} L^{-d}.$$

In particular, Z_V converges to zero (at least) with the CLT scaling. Thus, if the autocorrelation function h decays to zero sufficiently rapidly, a CLT scaling is ensured. For slower decorrelations, inferior convergence rates may be expected.

For the problem at hand, we are interested in $Z = \chi$, the characteristic function of the random inclusions. Then, we calculate

$$\mu = \phi \quad \text{and} \quad \sigma^2 = \phi(1 - \phi)$$

in terms of the particle volume fraction ϕ . Also, in terms of the identification $\phi_L^{\text{sn}} = \chi_{Q_L}$, the equation (5.2) becomes

$$\text{Var}(\phi_L^{\text{sn}}) = \phi(1 - \phi) \int_{Q_L} \int_{Q_L} h(x-y) dx dy. \quad (5.4)$$

For spherical inclusions, we investigate the autocorrelation function h more closely, cf. Fig. 13. Indeed, if the autocorrelation function h has a sufficiently rapid decay, the volume fraction ϕ_L of the snapshot will decay (at least) with the CLT scaling. Conversely, a non-CLT scaling must be rooted in slowly decaying decorrelations.

We considered cells with 32^3 spheres at $\phi = 30\%$ as our point of departure, fixed their size and reduced the generated volume fractions. The resulting *empirical* autocorrelation functions, for a single realization and computed by an FFT-based approach [62], are shown in Fig. 13(a). The autocorrelation function h at x provides the probability of finding an inclusion both at y and $y+x$ (averaged over y). As we consider only statistically isotropic ensembles, the autocorrelation function depends only on the magnitude $\|x\|$ of the vector x . Thus, the oscillations in Fig. 13(a) indicate closely packed spheres with a minimum

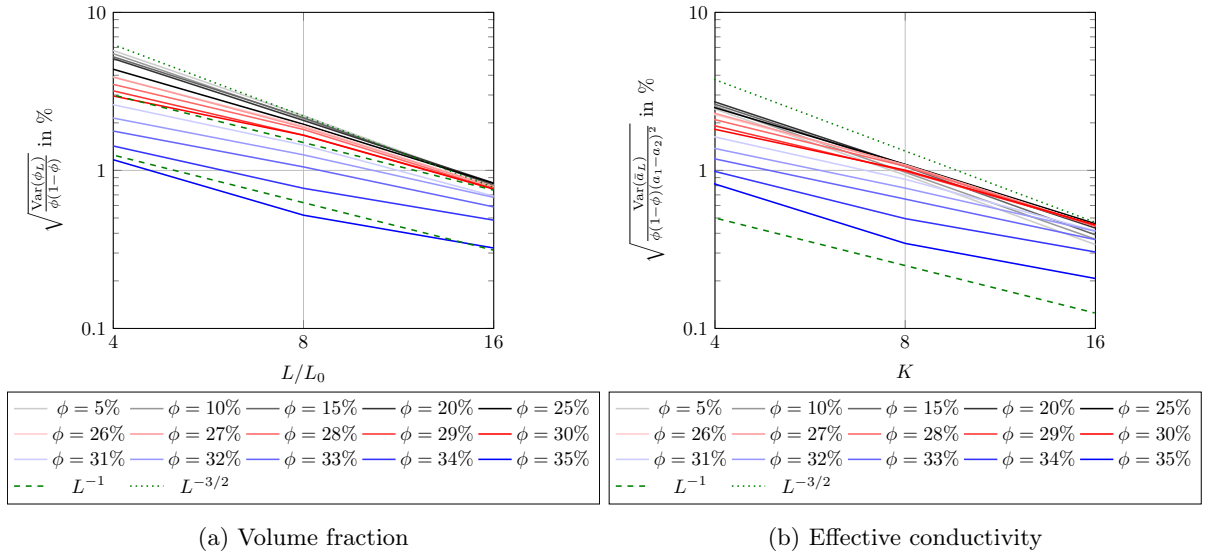


Figure 14: Normalized standard deviation of the volume fraction and the effective conductivity for spherical particles

distance between them. This is a result of the enforced minimum distance between the inclusions. With this interpretation in mind, Fig. 13(a) may be inspected more closely. For increasing volume fraction, the number of "links" in closely packed "chains" of spheres increases. Indeed, even for $\phi = 20\%$, only two spheres will be found in the vicinity of a fixed sphere. The third next sphere will be further apart already. For $\phi = 30\%$, already seven spheres are found close to a given sphere. For comparison, we also included the $\phi = 35\%$ case, which is even more highly packed. Actually, it was not possible to generate $\phi = 40\%$ with the MCM method. Indeed, due to the 20% isolation distance, we generate packings of spheres with a larger radius, and down-scale those spheres only in post-processing. For 20% isolation distance and a volume fraction $\phi = 40\%$, we would be generating sphere packings without isolation distance and a volume fraction $\phi = 1.2^3 \times 40\% = 69.12\%$. This number exceeds the jamming limit for spheres in three dimensions, and is thus extremely difficult, if not possible, to be realized by a random packing.

To assess the reliability of the computed autocorrelation functions, we computed ten realizations of the empirical autocorrelation functions for 64^3 spheres at 30% volume fraction, and considered the mean and standard deviation of these samples, cf. Fig. 13(b). Notice that the mean autocorrelation function reaches the level of the standard deviation for about ten sphere radii and at a level of about 10^{-3} . Thus, the actual decay rate of the autocorrelation function cannot be identified from *these* numerical investigations. Thus, we turn our attention to equation (5.4), and assess the normalized quantity

$$\sqrt{\frac{\text{Var}(\phi_L^{\text{sn}})}{\phi(1-\phi)}} = \sqrt{\int_{Q_L} \int_{Q_L} h(x-y) dx dy}. \quad (5.5)$$

directly. For increasing volume fraction, the normalized standard deviation (5.5) is shown in Fig. 14(a), where we introduced a reference length scale L_0 , s.t. at $\phi = 30\%$, exactly $(L/L_0)^d$ spheres fit inside a cell with volume L^d to realize this volume fraction. Thus, L/L_0 is identical to the parameter K used previously, but also makes sense for other values of the filler fraction ϕ . Please note that we only ran 1000 simulations to cover the great variety of considered volume fractions.

Interestingly, up to a volume fraction of 20%, the normalized standard deviation is independent of the volume fraction and decays as predicted by the CLT. Thus, we observe a regime of rapid decorrelation. Increasing the volume fraction further, in particular from 25% to 30%, leads to an incremental change

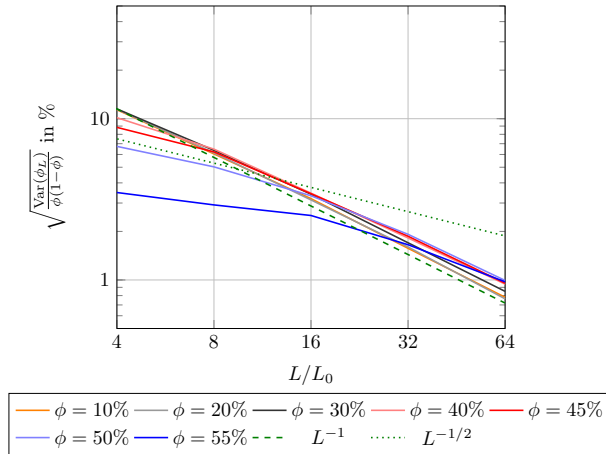


Figure 15: Normalized standard deviation of the area fraction for circular inclusions

in the convergence rate, continuously changing from the CLT scaling to a $1/L$ -rate. In Section 4.2, we considered precisely this regime. Increasing the volume fraction even further retains the $1/L$ -rate, but leads to an overall decrease of the standard deviation. Thus, we observe a regime with slow decorrelation but decreased variance due to an increased degree of spatial order.

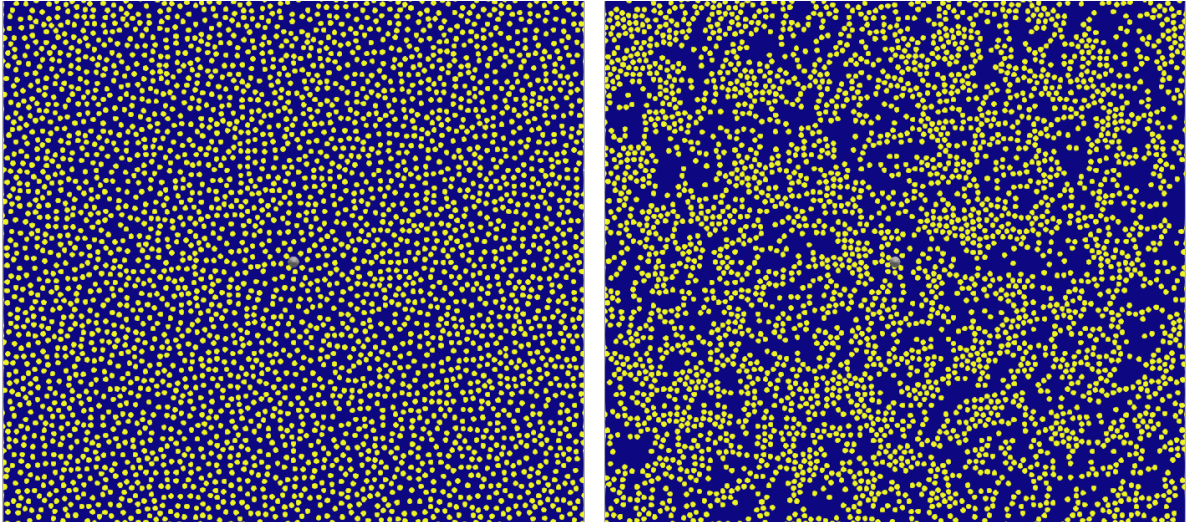
The corresponding empirically computed, normalized standard deviation of the effective conductivity is shown in Fig. 14(b). Similar to the volume fraction, different regimes emerge, corresponding to rapidly decorrelating ensembles which a favorable convergence rate (slightly inferior than CLT) and ensembles with long-range order, and an associated $1/L$ -decay.

Motivated by these observations, we turn to the two-dimensional case of circular inclusions. For spherical inclusions, the observed decay rate deteriorates close to the maximum packing fraction (accounting for the minimum distance). Thus, we similarly increased the packing area fraction for the circular inclusions, cf. Fig. 15. Using the MCM algorithm, area fractions up to $\phi = 55\%$ could be reached. Thus, in contrast to the three-dimensional case, the area fraction $\phi = 30\%$ considered in Section 4.3 is not even close to the maximum packing fraction. Thus, the corresponding normalized standard deviation of the snapshot area-fractions decay with the CLT scaling. Only for much higher area fractions, at about $\phi = 50\%$, an inferior decay rate of $L^{-\frac{1}{2}}$ appears. Interestingly, in such cases, there is a transition from a $L^{-\frac{1}{2}}$ -scaling up to $K = 16$ to the expected L^{-1} -scaling for larger cells.

It appears reasonable that such a transition to the standard CLT scaling should also appear for spherical and cylindrical fillers in three spatial dimension. However, the necessary size of the volume elements exceeds current computational capacities. Hence, we cannot observe it in this study.

These guesses on a CLT scaling for sufficiently large cells can also be backed up by theory. Indeed, Jeulin [63] showed that codimension- k linear varieties randomly dispersed in \mathbb{R}^d may lead to an L^{d-k} -scaling of the variance. Willot [64] demonstrated that, for cylindrical fibers at low volume fraction, two scaling regimes for the variance of the volume fraction are observed. Indeed, for small cells, the fibers appear infinitely long, and an L^{-1} -scaling arises. For sufficiently large cells, larger than about ten [64, Sec. 4.3] times the fiber length, the fibers are "small" compared to the volume, and the expected CLT scaling is recovered.

For the spherical and the circular fillers, a similar behavior is observed. Indeed, due to the microstructure generation process, the individual fillers interact in chains, or even networks of chains, cf. Fig. 3. Thus, one-dimensional structures arise. The average length of these structures depends on the target volume



(a) Random sequential addition (RSA) [46]

(b) Mechanical contraction method (MCM) [32]

Figure 16: Visual comparison of two cells with $64^2 = 4096$ circular inclusions at $\phi = 30\%$ area fraction, generated by two different algorithms

fraction, and, in turn, determines the decay behavior, cf. Fig. 14(a). The situation is visualized in Fig. 16. We compare two microstructures with the same microstructure parameters, but generated by different algorithms. The vanilla RSA method, see Fig. 16(a), leads to a configuration with a much more homogeneous appearance. In contrast, the MCM tends to form clusters, see Fig. 16(b). This does not come unexpected. Please recall that there is a well-defined jamming limit for RSA, which limits the expected volume fraction to be reached. At this jamming limit, the microstructures attain a rather homogeneous appearance, essentially due to a lack of non-occupied spots.

In contrast, the MCM is a *collective re-arrangement* algorithm which permits reaching much larger volume fractions than the RSA. It will also reach some sort of uniform jamming state, but at a much higher filler content.

Returning to the *real* material, of course, we cannot ab initio decide which microstructure generation method is suitable for the microstructured material at hand. However, for matrix-inclusion composites with industrial filler content, we expect collective re-arrangement algorithms to be more appropriate. Indeed, sequential algorithms like RSA place the inclusions in a successive fashion. In particular, the correlation length of the emerging ensemble is on the order of the inclusion size, independent of the filler fraction. At high filler content, and also motivated by the real production processes, the individual particles are expected to actually affect their neighbors. Indeed, for instance during injection molding, the filler particles interact with each other, both, in terms of hydrodynamic interactions, and in terms of direct particle-particle collisions. Thus, the correlation length of the produced microstructured materials actually depends on the filler content, and may cover a few particle sizes for high volume fraction.

To sum up, the observed inferior decay of the random error for the cut microstructures is a consequence of slowly decaying correlations between the particles in the ensemble. The latter are expected to emerge at high filler content, independently of the microstructure generation algorithm, used. Still, homogenization theory applies as long as the considered volume elements are large compared to the correlation length. Furthermore, in three dimensions and for the considered ensembles, we were unable to work on sufficiently large volume elements to reach the regime of the classical CLT scaling.

6 Conclusion

This work was devoted to sampling strategies for representative volume elements of matrix-inclusion composites.

From an engineering point of view, this article may be viewed as a natural continuation of the investigations of Kanit et al. [3], who introduced statistical terminology and methods for estimating a suitable RVE size. In contrast to Kanit et al. [3], who studied Voronoi tessellations with seeds distributed according to a Poisson point process, we were concerned with matrix-inclusion composites, i.e., we investigated circular, spherical and cylindrical fillers embedded in polymer matrices. In the engineering literature, attention is typically paid to the type of boundary conditions used for the corrector field on the RVE, i.e., whether Dirichlet, Neumann, periodic or mixed boundary conditions are imposed at the cell boundary [3]. For the article at hand, we focused on the treatment of particles at the cell boundary. Indeed, digital volume images of microstructures, which are available at high resolutions, see Bargmann et al. [5] for an overview for different types of microstructures, extract a sample from a component typically by either cutting or piercing - which we call taking a snapshot in the manuscript at hand. In particular, the resulting microstructures will not be periodic, and particles at the cell boundary are treated "improperly", even when imposing periodic boundary conditions. We could quantify the error introduced by taking snapshots to be rather high, both in terms of the systematic *and* the random error. The next logical step would be to investigate appropriate measures to counter-balance this effect, for instance by statistical methods [65] or modified correctors [21,22]. Also, the investigations underlined the importance of proper microstructure-generation tools [5], *even if digital images are available*. Put differently, it is strongly recommended to periodize the ensemble, and not only the snapshot.

In view of the work of Kanit et al. [3], we could confirm their observation that the systematic error for periodized ensembles does not exceed the random error, at least for the material contrast considered, so that the random error is a good indicator for the total RVE error.

We chose to work with thermal conductivity and a small material contrast to show the high probabilities for failing to produce accurate predictions of effective quantities, emphasizing that already for this seemingly innocent scenario, using the naive snapshot strategy may be suboptimal. Investigating higher material contrast and mechanical problems, in particular inelastic problems, is of immediate engineering interest. Groundwork was already laid by Kanit et al. [3], who reported an inferior convergence rate for the random error associated to mechanical problems. Also, Kanit et al. [3] argued that the random error scales as the material contrast, which remains to be confirmed by theoretical means.

Moreover, it would be interesting to investigate what happens for *long* fibers. In this work, we investigated short and continuous, i.e., infinitely long and aligned, fibers, but did not account for the intermediate regime expected in the presence of long fibers. In that case, RVEs with tractable complexity need to be significantly smaller than the fiber length, so that constructing periodized ensembles appears difficult.

To conclude the engineering perspective, let us highlight the importance of stochastic notions for working with RVEs in practice. Typically, emphasis is put on balancing computational effort and accuracy. For instance, if optimal scaling in the degrees of freedom is desired, one could either compute on eight cells of size Q_L or a *single* cell of size Q_{2L} in three spatial dimensions. However, there is an often neglected advantage of working with smaller cells - they provide an error estimator free of extra charge. Indeed, based on the empirical variance, in addition to the computed mean value, also a confidence interval may be estimated. Assuming the systematic error to be small compared to the random error, the latter confidence interval also provides an estimate for the error relative to the effective property of the infinite medium. In contrast, using only a single computation on the larger cell does not permit such an error analysis.

From the viewpoint of mathematical analysis, this article is a natural continuation of previous work by Khoromskaia et al. [26,27], where quantitative homogenization results for random media were confirmed by numerical simulations. Indeed, we go beyond the cited work by investigating microstructure models of higher complexity, as is required for engineering applications. In particular, we break into terrain previously uncharted from a theoretical point of view. The ensemble which we studied differs from the simpler one of independently drawing particles conditioned on no overlap. The former permits to reach higher volume fraction than the latter, in general, which is a desirable property for engineering applications. As the studied ensemble reveals a cross-over in the error scaling at a volume-fraction dependent intermediate length scale, it appears interesting to investigate this ensemble in more detail.

As quantitative stochastic homogenization crucially relies upon quantitative versions of ergodicity, typically in the form of functional inequalities in probability, it may be of interest to study which conditions hold for the ensembles considered in this work, see Duerinckx-Gloria [28,29] for investigations covering Poisson-Voronoi tessellations, as treated by Kanit et al. [3], and random sequential adsorption. In a similar direction, it might be interesting to study the intermediate length scale below which the convergence rate of the random error is inferior for snapshots of matrix-inclusion composites.

Modified corrector problems [22,66] aim to upgrade the decay of the systematic error to the level of the random error, but typically assume a CLT scaling of the random error. For the studied matrix-inclusion composites and the snapshot protocol, a strictly inferior decay of the random error was observed in an intermediate regime for high filler fraction and moderate cell sizes. It appears sensible to investigate whether those methods that modify the corrector equation [21,66] improve the decay of the random error for such ensembles, as well.

As opposed to Khoromskaia et al. [26], we could not (yet) confirm the optimal convergence rate of the systematic error and properly periodized ensembles predicted by Clozeau et al. [24]. Computations on even larger cells could reveal the proper decay rate of the systematic error.

A cornerstone of the seminal paper of Kanit et al. [3] is the concept of integral range in spatial statistics [60,61], which quantifies the constant in front of the CLT scaling of a second-order stationary random field. In their study of the homogenization commutator, Duerinckx et al. [42] related the Q -tensor, introduced by Mourrat and coworkers [67,68], to the stochastic fluctuations of the apparent properties associated to RVEs. Due to the characterization [42, Thm. 2] in terms of a limiting procedure, the Q -tensor may be regarded as an extension of the integral range to stochastic homogenization, and a closer investigation appears desirable.

Last but not least, let us remark that it would be interesting to understand what happens at interfaces between different heterogeneous materials [69], for instance in recent technological lightweight applications where continuously and discontinuously reinforced plastics are combined [70].

Acknowledgments

M. Schneider was supported by the German Research Foundation (DFG) within the International Research Training Group "Integrated engineering of continuous-discontinuous long fiber reinforced polymer structures" (GRK 2078). M. Schneider thanks S. Gajek for computational support and H. Andr a for stimulating discussions.

This work was initiated while M. Josien held a post-doc position in the Max Planck Institute for Mathematics in the Sciences (MPI MiS), Leipzig.

A A series expansion for the effective thermal conductivity

In this appendix, we collect the arguments leading to the estimate (5.1)

$$\sqrt{\langle \|\bar{A} - A_L\|^2 \rangle} \leq 4\sqrt{\alpha_1\alpha_2}\sqrt{\text{Var}(\phi_L)}\rho + O(\rho^2)$$

for the convenience of the reader. Let us fix some positive definite reference thermal conductivity tensor A^0 . By algebraic manipulations, see Milton [71, Sec. 14.9], for fixed $\bar{\xi} \in \mathbb{R}^d$, the random vector field ξ solves the equations (2.2) and (2.3) precisely if $p = (A + A^0)\xi$ solves the Eyre-Milton equation [55]

$$(\text{Id} - YZ^0)p = 2A^0\bar{\xi} \quad (\text{A.1})$$

involving the Helmholtz reflection $Y = \text{Id} - 2\Gamma$ and the Cayley mapping $Z^0 = (A - A^0)(A + A^0)^{-1}$. As the reflection Y is orthogonal and Z^0 is an L^2 -contraction provided the coefficient field A is essentially bounded and uniformly positive definite [55], the polarization p solving the Eyre-Milton equation (A.1) may be represented in terms of a Neumann series

$$p = 2 \sum_{k=0}^{\infty} (YZ^0)^k A^0\bar{\xi} \quad (\text{A.2})$$

with corresponding expectation

$$\langle p \rangle = 2 \sum_{k=0}^{\infty} \langle (YZ^0)^k A^0\bar{\xi} \rangle.$$

Taking into account $p = q + A^0\xi$, we obtain

$$\bar{A}\bar{\xi} + A^0\bar{\xi} = 2A^0\bar{\xi} + 2\langle YZ^0 A^0\bar{\xi} \rangle + 2 \sum_{k=2}^{\infty} \langle (YZ^0)^k A^0\bar{\xi} \rangle,$$

i.e., using that the expectation vanishes on the image of the Helmholtz projector Γ ,

$$\bar{A}\bar{\xi} = A^0\bar{\xi} + 2\langle Z^0 A^0\bar{\xi} \rangle + 2 \sum_{k=2}^{\infty} \langle (YZ^0)^k A^0\bar{\xi} \rangle, \quad (\text{A.3})$$

To proceed, we restrict our attention to two-phase isotropic composites, i.e., we suppose that the thermal conductivity tensor takes the form

$$A = \alpha_1\chi \text{Id} + \alpha_2(1 - \chi) \text{Id} \quad (\text{A.4})$$

in terms of non-vanishing isotropic heat conductivities α_1 as well as α_2 and the indicator function χ of a random set. Define $A^0 = \alpha_0 \text{Id}$ with $\alpha_0 = \sqrt{\alpha_1\alpha_2}$. Then,

$$Z^0 = (A - A^0)(A + A^0)^{-1} = \frac{\alpha_1 - \alpha_0}{\alpha_1 + \alpha_0}\chi \text{Id} + \frac{\alpha_2 - \alpha_0}{\alpha_2 + \alpha_0}(1 - \chi) \text{Id} = \frac{\sqrt{\alpha_1} - \sqrt{\alpha_2}}{\sqrt{\alpha_1} + \sqrt{\alpha_2}}[\chi - (1 - \chi)] \text{Id},$$

i.e.,

$$Z^0 = \rho(2\chi - 1) \text{Id} \quad \text{with} \quad \rho = \frac{\sqrt{\alpha_1} - \sqrt{\alpha_2}}{\sqrt{\alpha_1} + \sqrt{\alpha_2}} \in (-1, 1).$$

Inserting the latter expression into the Neumann series (A.3), we obtain

$$\bar{A}\bar{\xi} = \sqrt{\alpha_1\alpha_2}\bar{\xi} + 2\sqrt{\alpha_1\alpha_2}\rho(2\langle \chi \rangle - 1)\bar{\xi} + 2\sqrt{\alpha_1\alpha_2} \sum_{k=2}^{\infty} \langle (YZ^0)^k \bar{\xi} \rangle,$$

which we might also write in the form

$$\bar{A}\bar{\xi} = \sqrt{\alpha_1\alpha_2}(1 - 2\rho)\bar{\xi} + 4\sqrt{\alpha_1\alpha_2}\rho\langle\chi\rangle\bar{\xi} + O(\rho^2).$$

We recover the known result, see Milton [71, Ch. 14], that, to first order in ρ , the volume fraction $\phi \equiv \langle\chi\rangle$ determines the effective conductivity.

For the snapshot ensemble on the cell Q_L , an analogous argument yields the representation

$$\bar{A}_L^{\text{sn}} = \sqrt{\alpha_1\alpha_2}(1 - 2\rho)\bar{\xi} + 4\sqrt{\alpha_1\alpha_2}\rho\phi_L^{\text{sn}}\bar{\xi} + O(\rho^2),$$

where the constant in the Landau- O depends on L and the snapshot volume-fraction ϕ_L^{sn} is a random variable determined by

$$\phi_L^{\text{sn}} = \int_{Q_L} \chi dx.$$

The snapshot volume-fraction ϕ_L^{sn} leads to an unbiased estimator for the volume fraction ϕ , i.e.,

$$\langle\phi_L^{\text{sn}}\rangle = \phi$$

holds. In particular, the systematic error $\|\bar{A} - \bar{A}_L^{\text{sn}}\|$ is entirely determined by the ρ^2 -term. In contrast, the formula for the difference

$$\bar{A} - \bar{A}_L^{\text{sn}} = 4\sqrt{\alpha_1\alpha_2}(\phi - \phi_L^{\text{sn}})\rho \text{Id} + O(\rho^2)$$

permits bounding the random error in the form

$$\sqrt{\langle\|\bar{A} - \bar{A}_L^{\text{sn}}\|^2\rangle} \leq 4\sqrt{\alpha_1\alpha_2}\sqrt{\text{Var}(\phi_L^{\text{sn}})}\rho + O(\rho^2). \quad (\text{A.5})$$

In particular, the random error is, up to first order in the material contrast dependent parameter ρ , determined by the standard deviation of the snapshot volume-fraction ϕ_L^{sn} . We close this Section with a remark: The expansion (5.1) also holds in case of the periodized ensemble A_L^{per} . If the latter is constructed in such a way that the associated volume fraction for specific L is such that $\phi_L^{\text{per}} = \phi$ holds, the linear term in ρ will vanish for the standard-deviation expansion (5.1), i.e., the random error may be expected to become smaller. The latter idea has been extended to higher-order terms by Le Bris et al. [72] and analyzed by Fischer [73].

References

- [1] R. Hill, “Elastic properties of reinforced solids: Some theoretical principles,” *Journal of the Mechanics and Physics of Solids*, vol. 11, no. 5, pp. 357–372, 1963.
- [2] W. J. Drugan and J. R. Willis, “A micromechanics-based nonlocal constitutive equations and estimates of representative volume element size for elastic composites,” *Journal of the Mechanics and Physics of Solids*, vol. 44, pp. 497–524, 1996.
- [3] T. Kanit, S. Forest, I. Galliet, V. Mounoury, and D. Jeulin, “Determination of the size of the representative volume element for random composites: statistical and numerical approach,” *Journal of the Mechanics and Physics of Solids*, vol. 40, no. 13–14, pp. 3647–3679, 2003.
- [4] K. Matouš, M. G. D. Geers, V. G. Kouznetsova, and A. Gillman, “A review of predictive nonlinear theories for multiscale modeling of heterogeneous materials,” *Journal of Computational Physics*, vol. 330, pp. 192–220, 2017.
- [5] S. Bargmann, B. Klusemann, J. Markmann, J. E. Schnabel, K. Schneider, C. Soyarslan, and J. Wilmers, “Generation of 3D representative volume elements for heterogeneous materials: A review,” *Progress in Materials Science*, vol. 96, pp. 322–384, 2018.
- [6] E. N. Landis and D. T. Keane, “X-ray microtomography,” *Materials Characterization*, vol. 61, pp. 1305–1316, 2010.

- [7] I. Guven and K. Cinar, “Micromechanical modeling of particulate-filled composites using micro-CT to create representative volume elements,” *International Journal of Mechanics and Materials in Design*, vol. 15, pp. 695–714, 2019.
- [8] E. di Giorgi and S. Spagnolo, “Sulla convergenza degli integrali dell’energia per operatori ellittici del secondo ordine,” *Annali della Scuola Normale Superiore di Pisa*, vol. 8, pp. 391 – 411, 1973.
- [9] I. Babuska, “Solution of interface problems by homogenization I,” *SIAM Journal on Mathematical Analysis*, vol. 7, pp. 603–634, 1973.
- [10] E. Larsen, “Neutron transport and diffusion in inhomogeneous media,” *Journal of Mathematical Physics*, vol. 16, pp. 1421–1427, 1975.
- [11] G. C. Papanicolaou and S. R. S. Varadhan, “Boundary value problems with rapidly oscillating random coefficients,” in *Random fields, Vol. I, II (Esztergom, 1979)*, vol. 27 of *Colloq. Math. Soc. János Bolyai*, pp. 835–873, North-Holland, Amsterdam-New York, 1981.
- [12] S. M. Kozlov, “Averaging of differential operators with almost periodic rapidly oscillating coefficients,” *Mathematics of the USSR-Sbornik*, vol. 107 (149), no. 2 (10), pp. 199–217, 1978.
- [13] A. Gloria, S. Neukamm, and F. Otto, “Quantification of ergodicity in stochastic homogenization: optimal bounds via spectral gap on Glauber dynamics,” *Inventiones mathematicae*, vol. 199, no. 2, pp. 455–515, 2015.
- [14] A. Bourgeat and A. Piatnitski, “Approximations of effective coefficients in stochastic homogenization,” *Annales de l’Institut H. Poincaré*, vol. 40, pp. 153–165, 2004.
- [15] H. Owhadi, “Approximation of the effective conductivity of ergodic media by periodization,” *Probability Theory and Related Fields*, vol. 125, pp. 225–258, 2003.
- [16] A. Egloffé, A. Gloria, J.-C. Mourrat, and T. N. Nguyen, “Random walk in random environment, corrector equation and homogenized coefficients: from theory to numerics, back and forth,” *IMA Journal of Numerical Analysis*, vol. 35, no. 2, pp. 499–545, 2015.
- [17] T. Y. Hou and X.-H. Wu, “A Multiscale Finite Element Method for Elliptic Problems in Composite Materials and Porous Media,” *Journal of Computational Physics*, vol. 134, pp. 169–189, 1997.
- [18] W. E, P. Ming, and P. Zhang, “Analysis of the heterogeneous multiscale method for elliptic homogenization problems,” *Journal of the American Mathematical Society*, vol. 18, no. 1, pp. 121–156, 2005.
- [19] X. Blanc and C. Le Bris, “Improving on computation of homogenized coefficients in the periodic and quasi-periodic settings,” *Networks and Heterogeneous Media*, vol. 5, no. 1, pp. 1–29, 2010.
- [20] A. Gloria, “Reduction of the resonance error - Part 1: Approximation of homogenized coefficients,” *Mathematical Models and Methods in Applied Sciences*, vol. 21, no. 8, pp. 1601–1630, 2011.
- [21] A. Abdulle, D. Arjmand, and E. Paganoni, “Exponential decay of the resonance error in numerical homogenization via parabolic and elliptic cell problems,” *Comptes Rendus Mathématique*, vol. 357, no. 6, pp. 545–551, 2019.
- [22] J. Mourrat, “Efficient Methods for the Estimation of Homogenized Coefficients,” *Foundations of Computational Mathematics*, vol. 19, pp. 435–483, 2019.
- [23] D. Arjmand and O. Runborg, “A time dependent approach for removing the cell boundary error in elliptic homogenization problems,” *Journal of Computational Physics*, vol. 341, pp. 206–227, 2016.
- [24] N. Clozeau, M. Josien, F. Otto, and Q. Xu, “Bias in the Representative Volume Element method: periodize the ensemble instead of its realizations,” 2021. in preparation.
- [25] A. Gloria, “An analytical framework for numerical homogenization. II. Windowing and oversamplings,” *Multiscale Modeling & Simulation*, vol. 7, no. 1, pp. 274–293, 2008.
- [26] V. Khoromskaia, B. N. Khoromskij, and F. Otto, “Numerical study in stochastic homogenization for elliptic partial differential equations: Convergence rate in the size of representative volume elements,” *Numerical Linear Algebra and Applications*, vol. 27, p. e2296, 2020.
- [27] V. Khoromskaia and B. N. Khoromskij, “Tensor-based techniques for fast discretization and solution of 3D elliptic equations with random coefficients,” *arXiv:2007.06524*, pp. 1–25, 2020.
- [28] M. Duerinckx and A. Gloria, “Weighted functional inequalities: Constructive approach,” *hal-01633041*, pp. 1–45, 2017.
- [29] M. Duerinckx and A. Gloria, “Multiscale functional inequalities in probability: Concentration properties,” *arXiv:1711.03148*, pp. 1–24, 2017.
- [30] H. Moulinec and P. Suquet, “A fast numerical method for computing the linear and nonlinear mechanical properties of composites,” *Comptes Rendus de l’Académie des Sciences. Série II*, vol. 318, no. 11, pp. 1417–1423, 1994.

- [31] H. Moulinec and P. Suquet, “A numerical method for computing the overall response of nonlinear composites with complex microstructure,” *Computer Methods in Applied Mechanics and Engineering*, vol. 157, pp. 69–94, 1998.
- [32] S. Williams and A. Philipse, “Random packings of spheres and spherocylinders simulated by mechanical contraction,” *Physical Reviews E*, vol. 67, pp. 1–9, 2003.
- [33] M. Schneider, “The Sequential Addition and Migration method to generate representative volume elements for the homogenization of short fiber reinforced plastics,” *Computational Mechanics*, vol. 59, pp. 247–263, 2017.
- [34] V. V. Zhikov, S. M. Kozlov, and O. A. Oleinik, *Homogenization of Differential Operators and Integral Functionals*. New York: Springer-Verlag, 1994.
- [35] A. Gloria and F. Otto, “Quantitative estimates on the periodic approximation of the corrector in stochastic homogenization,” *ESAIM: Proceedings and Surveys*, vol. 48, pp. 80–97, 2016.
- [36] C. Huet, “Application of variational concepts to size effects in elastic heterogeneous bodies,” *Journal of the Mechanics and Physics of Solids*, vol. 38, pp. 813–841, 1990.
- [37] K. Sab, “On the homogenization and the simulation of random materials,” *European Journal of Mechanics A-solids*, vol. 11, pp. 585–607, 1992.
- [38] S. N. Armstrong and C. K. Smart, “Quantitative stochastic homogenization of convex integral functionals,” *Annales Scientifiques de l’Ecole Normale Supérieure*, vol. 49, no. 2, pp. 423–481, 2016.
- [39] S. N. Armstrong and J.-C. Mourrat, “Lipschitz regularity for elliptic equations with random coefficients,” *Archive for Rational Mechanics and Analysis*, vol. 219, pp. 255–346, 2016.
- [40] V. V. Yurinskii, “Averaging of symmetric diffusion in random medium,” *Siberian Mathematical Journal*, vol. 27, pp. 603–613, 1986.
- [41] A. Naddaf and T. Spencer, “Estimates On the Variance of Some Homogenization Problems,” *Unpublished Preprint*, pp. 1–14, 1998.
- [42] M. Duerinckx, A. Gloria, and F. Otto, “The Structure of Fluctuations in Stochastic Homogenization,” *Communications in Mathematical Physics*, vol. 377, pp. 259–306, 2020.
- [43] S. Torquato, *Random Heterogeneous Materials – Microstructure and Macroscopic Properties*. New York: Springer, 2002.
- [44] J. Fischer and F. Otto, “Sublinear growth of the corrector in stochastic homogenization: optimal stochastic estimates for slowly decaying correlations,” *Stochastics and Partial Differential Equations: Analysis and Computations*, vol. 5, pp. 220–255, 2017.
- [45] A. Gloria, S. Neukamm, and F. Otto, “Quantitative estimates in stochastic homogenization for correlated coefficient fields,” *arXiv:1910.05530*, pp. 1–39, 2019.
- [46] J. Feder, “Random sequential adsorption,” *Journal of Theoretical Biology*, vol. 87, no. 2, pp. 237–254, 1980.
- [47] P. Meakin, “Random sequential adsorption of spheres of different sizes,” *Physica A*, vol. 187, no. 3, pp. 475–488, 1992.
- [48] B. D. Lubachevsky and F. H. Stillinger, “Geometric Properties of Random Disk Packings,” *Journal of Statistical Physics*, vol. 60, no. 5–6, pp. 561–583, 1990.
- [49] S. Torquato and Y. Jiao, “Robust algorithm to generate a diverse class of dense disordered and ordered sphere packings via linear programming,” *Physical Reviews E*, vol. 82, no. 6, p. 061302, 2010.
- [50] W. Mattson and B. M. Rice, “Near-neighbor calculations using a modified cell-linked list method,” *Computer Physics Communications*, vol. 119, pp. 135–148, 1999.
- [51] C. Dorn and M. Schneider, “Lippmann-Schwinger solvers for the explicit jump discretization for thermal computational homogenization problems,” *International Journal for Numerical Methods in Engineering*, vol. 118, no. 11, pp. 631–653, 2019.
- [52] J. Vondřejc, J. Zeman, and I. Marek, “An FFT-based Galerkin method for homogenization of periodic media,” *Computers & Mathematics with Applications*, vol. 68, no. 3, pp. 156–173, 2014.
- [53] S. Brisard and L. Dormieux, “Combining Galerkin approximation techniques with the principle of Hashin and Shtrikman to derive a new FFT-based numerical method for the homogenization of composites,” *Computer Methods in Applied Mechanics and Engineering*, vol. 217 – 220, pp. 197 – 212, 2012.
- [54] M. Schneider, “Convergence of FFT-based homogenization for strongly heterogeneous media,” *Mathematical Methods in the Applied Sciences*, vol. 38, no. 13, pp. 2761–2778, 2015.
- [55] D. J. Eyre and G. W. Milton, “A fast numerical scheme for computing the response of composites using grid refinement,” *The European Physical Journal - Applied Physics*, vol. 6, no. 1, pp. 41–47, 1999.

- [56] M. Schneider, D. Wicht, and T. Böhlke, “On polarization-based schemes for the FFT-based computational homogenization of inelastic materials,” *Computational Mechanics*, vol. 64, no. 4, pp. 1073–1095, 2019.
- [57] M. Schneider, “On the Barzilai-Borwein basic scheme in FFT-based computational homogenization,” *International Journal for Numerical Methods in Engineering*, vol. 118, no. 8, pp. 482–494, 2019.
- [58] S. G. Advani and C. L. Tucker, “The Use of Tensors to Describe and Predict Fiber Orientation in Short Fiber Composites,” *Journal of Rheology*, vol. 31, no. 8, pp. 751–784, 1987.
- [59] V. Müller, M. Kabel, H. Andrä, and T. Böhlke, “Homogenization of linear elastic properties of short fiber reinforced composites – A comparison of mean field and voxel-based methods,” *International Journal of Solids and Structures*, vol. 67–68, pp. 56–70, 2015.
- [60] G. Matheron, *Estimating and Choosing*. Berlin: Springer, 1989.
- [61] C. Lantuéjoul, *Geostatistical Simulation - Models and Algorithms*. Berlin: Springer, 2002.
- [62] D. T. Fullwood, S. R. Niezgodna, and S. R. Kalidindi, “Microstructure reconstructions from 2-point statistics using phase-recovery algorithms,” *Acta Materialia*, vol. 56, no. 5, pp. 942–948, 2008.
- [63] D. Jeulin, “Power Laws Variance Scaling of Boolean Random Varieties,” *Methodology and Computing in Applied Probability*, vol. 18, no. 4, pp. 1065–1079, 2016.
- [64] F. Willot, “Mean Covariogram of Cylinders and Applications to Boolean Random Sets,” *Journal of Contemporary Mathematical Analysis (Armenian Academy of Sciences)*, vol. 52, no. 6, pp. 305–315, 2017.
- [65] J. Ohser and F. Mücklich, *Statistical Analysis of Microstructures in Materials Science*. New York: Wiley, 2000.
- [66] A. Gloria and Z. Habibi, “Reduction in the Resonance Error in Numerical Homogenization II: Correctors and Extrapolation,” *Foundations of Computational Mathematics*, vol. 16, pp. 217–296, 2016.
- [67] Y. Gu and J.-C. Mourrat, “Scaling limit of fluctuations in stochastic homogenization,” *Multiscale Modeling and Simulation*, vol. 14, no. 1, pp. 452–481, 2016.
- [68] J.-C. Mourrat and F. Otto, “Correlation structure of the corrector in stochastic homogenization,” *Annals of Probability*, vol. 44, no. 5, pp. 3207–3233, 2016.
- [69] M. Josien and C. Raithel, “Quantitative homogenization for the case of an interface between two heterogeneous media,” *SIAM Journal on Mathematical Analysis*, vol. 53, pp. 813–854, 2021.
- [70] J. Görthofer, N. Meyer, T. D. Pallicity, L. Schöttl, A. Trauth, M. Schemmann, M. Hohberg, P. Pinter, P. Elsner, F. Henning, A. Hrymak, T. Seelig, K. Weidenmann, L. Kärger, and T. Böhlke, “Virtual process chain of sheet molding compound: Development, validation and perspectives,” *Composites Part B: Engineering*, vol. 169, pp. 133–147, 2019.
- [71] G. W. Milton, *The Theory of Composites*. Cambridge: Cambridge University Press, 2002.
- [72] C. Le Bris, F. Legoll, and M. Minvielle, “Special quasirandom structures: A selection approach for stochastic homogenization,” *Monte Carlo Methods and Applications*, vol. 22, no. 1, pp. 25–54, 2016.
- [73] J. Fischer, “The choice of representative volumes in the approximation of effective properties of random materials,” *Archive of Rational Mechanics and Analysis*, vol. 234, no. 2, pp. 635–726, 2019.